Electron Identification and $ZZ \rightarrow 4\ell(e, \mu)$ Cross Section Measurement with the CMS Detector

by

Michael Ryan Mooney

Submitted to the Department of Physics
in partial fulfillment of the requirements for the degree of

Bachelor of Science

at the

MASSACHUSETTS INSTITUTE OF TECHNOLOGY
[June 2008]
May 2008

Author .....
Department of Physics
May 9, 2008

Certified by .....
Christoph M. E. Paus
Associate Professor
Thesis Supervisor

Accepted by .....
David E. Pritchard
Senior Thesis Coordinator, Department of Physics

Electron Identification and $ZZ \rightarrow 4\ell(e, \mu)$ Cross Section Measurement with the CMS Detector

by

Michael Ryan Mooney

Submitted to the Department of Physics
on May 9, 2008, in partial fulfillment of the
requirements for the degree of
Bachelor of Science

Abstract

We perform multiple analyses using generator-level information in the Compact Muon Solenoid (CMS) detector at the Large Hadron Collider (LHC). In particular, we carry out three central investigations: the determination of electron efficiencies, electron fake rates, and $ZZ \rightarrow 4\ell(e, \mu)$ cross sections. Reconstructed Z boson decays are used as a benchmark in association with our cut-based analysis. In the $Z \rightarrow 2e$ channel we find an overall electron efficiency of $77.0\% \pm 1.3\%$, and electron fake rates are calculated to be $(1.7 \pm 0.5) \cdot 10^{-3}$ and $(0.6 \pm 0.2) \cdot 10^{-3}$ for the photon jet and QCD channels, respectively. We calculate an expected total of 17 counts/fb^{-1} for $ZZ \rightarrow 4\ell$, which we find to have a cross section of $\sigma_{ZZ \rightarrow 4\ell} = 180 \pm 45 \pm 6$ fb (with statistical uncertainty listed before systematic uncertainty). From our analysis using generator-level information, we obtain a set of reconstruction-level techniques that will be useful once the LHC starts delivering pp collisions sometime in 2008.

Thesis Supervisor: Christoph M. E. Paus
Title: Associate Professor

Acknowledgments

This MIT undergraduate thesis has been quite an endeavor and has required much input from a variety of people that I have worked with. Needless to say, I am very thankful for the help I have received from these people this past summer and over January at CERN. I would first like to thank my thesis supervisor, Professor Christoph Paus, for helping make arrangements for me coming to CERN twice as well as for his endless advice and humor. He has gone far out of his way to accommodate my stay in Switzerland, including lending me his apartment ("Paus Haus") and car ("Paus-mobile") for the summer. I am also very thankful that his car just happens to have automatic transmission, a rare thing to find in Europe.

Furthermore, I would have been unable to complete my thesis without the help of two research scientists, Markus Klute and Guillelmo Gomez-Ceballos. They devoted many hours this past summer to helping me with my analysis and educating me in particle physics in a way that could not possibly be mimicked in the classroom, despite having much work of their own to complete. Further thanks goes to Mike Miller and Jonatan Piedra for their suggestions, as well as Professor Bolek Wyslouch and Professor Steve Nahn for helping make my stay at CERN comfortable. I could not possibly leave out the graduate students, Pieter Everaerts, Yetkin Yilmaz, Phil Harris, Matt Rudolph, Kevin Sung, Steve Jaditz, and Josh Bendavid, who answered many questions of mine and made life at CERN and MIT interesting. Finally, I very much appreciate the help and friendship of my fellow MIT undergraduates, Philip Ilten and Constantinos Melachrinos, who worked with me often very late into the night.

Contents

Chapter 1

Introduction

The Large Hadron Collider (LHC) is expected to start operating at the European Particle Physics Laboratory, CERN (located near Geneva, Switzerland), in the summer of 2008. This proton-proton collider will function at a center-of-mass system energy of 14 TeV, providing a unique and exciting opportunity to study particle interactions at energies only approached before during the first few moments after the Big Bang [1], aside from cosmic rays. Such energies are almost a factor of ten higher than ever achieved in the laboratory before. Many physicists have eagerly awaited this chance to confirm or falsify the existence of the Higgs boson, a theoretical particle hypothesized in 1964 by Peter Higgs (along with François Englert and Robert Brout) that would explain the origin of electroweak symmetry breaking in Nature as well as account for the masses of all other elementary particles [2,3]. The discovery of such a particle would complete the Standard Model of particle physics [4–6]. However, it is very possible that physicists do not find the Higgs boson at the LHC but instead find the presence of new physics that resolve at higher energies. Such possible new phenomena include supersymmetry [7, 8], extra dimensions [9, 10], leptoquarks [11, 12], and small black holes [13, 14]. The reader can find a suitable introduction to the Standard Model and many of these topics in [15].

The Compact Muon Solenoid (CMS) experiment is one of the two general purpose detectors designed for the search for new physics at the LHC. The CMS experiment currently involves more than 2000 physicists from more than 150 institutes and 37 countries. These physicists contribute to detector development in terms of both hardware and software, taking part in detector performance testing, analysis preparation, and data operations concerning the large information flow through the detector once the LHC is operational (as well as Monte Carlo production in the meantime). Along with ATLAS (A Toroidal LHC Apparatus), CMS will study the high-energy proton-proton collisions of the LHC, sifting through billions of events to find rare collisions of great interest. Though these events may be small in number, they could very well completely reshape our understanding of space and matter for many years to come.

While there is currently no data available because the LHC is not yet running, we have access to Monte Carlo simulations of various different channels of proton-proton collisions within the CMS detector. These simulations are produced using PYTHIA [16] for collision modeling and Geant4 [17] for detector modeling. By completing analysis on these generator-level simulations, we have developed reconstruction-level techniques to be used once the LHC begins taking data. In this paper we focus primarily on a cross section measurement of the $ZZ \rightarrow 4\ell(e, \mu)$ channel, making use of a select variety of these Monte Carlo samples. In order to carry out this measurement, we must first concern ourselves with electron identification: determining electron efficiencies and fake rates. The efficiency of a lepton (such as an electron) is how often a real lepton is correctly identified within the detector, while the fake rate of a lepton is the rate at which the detector misidentifies a different particle as the lepton. These two quantities are essential to design an analysis involving leptons. Our interest in the $ZZ \rightarrow 4\ell(e, \mu)$ channel arises from the fact that it serves as the primary background to the $H \rightarrow ZZ \rightarrow 4\ell(e, \mu)$ discovery channel. We complete analysis on the former using simulation-level information in analogue to how we will analyze the

latter with actual data. This is done by treating the $ZZ \rightarrow 4\ell$ channel as a signal channel.

We begin by first discussing the Standard Model of particle physics and the underlying theory to the Higgs mechanism, which motivates the experimental search for the Higgs boson in efforts to unveil the mystery of mass. Alternate theories concerning new physics such as supersymmetry and others listed above are briefly discussed. The geometry and physics of the different parts of the CMS detector, including the tracker, electromagnetic calorimeter, hadron calorimeter, and muon chambers, are discussed at length as they play a role in understanding our analyses [18]. We then proceed to discuss electron efficiencies, electron fake rates, and the $ZZ \rightarrow 4\ell$ cross section measurement (including signal versus background optimization). These explanations incorporate discussions of the specific Monte Carlo samples used as well as additional studies related to electron identification and diboson analysis such as electron charge misidentification, faking particle identification, and jet content.

Chapter 2

Theory

In the last century, classical field theory, relativity, and quantum mechanics were combined together to create quantum field theory. This has led to many insights, such as the fact that each particle is required to have an antiparticle [19]. Progress in experimental high energy physics, through an exponential increase in available energy for the production of massive particles as a function of time [20], has led to many verifications of quantum field theory, leading to an established list of fundamental particles and their interactions known as the Standard Model of particle physics (SM). The SM includes a description of the electromagnetic, weak, and strong forces of Nature. The other great advance of the last century, general relativity, has resisted inclusion within the SM framework, and so the model does not contain gravity as a fundamental quantum theory. Regardless of being a complete theory of Nature, the SM is reaching its completion, lacking only the experimental discovery of the Higgs boson [2]. We will first explain the SM and the importance of the Higgs boson in this model, including possible alternative physics to the Standard Model.

2.1 Standard Model

The SM particles consist of spin-1/2 fermions (obeying Fermi-Dirac statistics) which are the matter particles and spin-1 bosons (obeying Bose-Einstein statistics) which are the force carriers that communicate the forces between the fermions. The fermions with only electroweak interactions (inclusive of the electromagnetic and weak interactions) are the charged leptons, which consist of the electron (e^-), muon (μ^-), and tau particle (τ^-), in order of increasing mass, along with their antiparticles. These particles each have charge -1, and the antiparticles have charge +1. The uncharged leptons are called neutrinos and interact only through the weak interaction. One neutrino exists for each charged lepton (ν_e, $\bar{\nu}_e$, ν_μ, $\bar{\nu}_\mu$, ν_τ, and $\bar{\nu}_\tau$), and all neutrinos have masses with upper limits that are measured to be very small [15].

The discovery of the constituents of hadronic matter, quarks, in deep inelastic scattering experiments [21–24] gave birth to quantum chromodynamics (QCD) as the generally accepted theory of strong interactions [25]. These fermions experience strong interactions in addition to the electroweak interactions that leptons experience. Over the past several decades, as the energy of particle beams in scattering experiments has increased, six different flavors of quarks have been found: up (u), down (d), strange (s), charmed (c), bottom (b), and top (t), in order of increasing mass. Each quark has a charge of +2/3 (u, c, and t quarks) or -1/3 (d, s, and b quarks). An additional property of the quark required by the Pauli exclusion principle was later introduced as color [26], allowing for three distinct versions of each quark: red (q_r), blue (q_b), and green (q_g). For antiquarks, this corresponds to antired ($\bar{q}_{\bar{r}}$), antiblue ($\bar{q}_{\bar{b}}$), and antigreen ($\bar{q}_{\bar{g}}$).

In QCD, two or three quarks can group together to form bound states (hadrons) as long as they are together colorless. This requires either a combination of three quarks or antiquarks with different colors (e.g. the proton, $u_r u_g d_b$) or a combination of one quark and one antiquark (e.g. the positively-charged pion, $u_r \bar{d}_{\bar{r}}$). The for-

mer combinations (qqq or $\bar{q}\bar{q}\bar{q}$) give rise to hadrons called baryons, while the latter combinations ($q\bar{q}$) give rise to hadrons referred to as mesons. The quarks are bound together by the strong force, exhibiting asymptotically free behavior [27,28]. In other words, quarks feel little force at small separations, but experience a powerful color charge binding force as they move apart. This is the reason that quarks only appear in colorless combinations, commonly referred to as confinement.

Lastly, we have the bosons, mitigating the interaction of the particles discussed above. The massless quanta of the electromagnetic field are called photons (γ), which together with the massive Z, W^+, and W^- bosons of the weak force, describe electroweak interactions. The strong interaction is mitigated by gluons (g), which contain color much like quarks. The last boson of the SM, the spin-0 Higgs boson (H), has not yet been discovered and its relevance is discussed in the following section.

2.2 Higgs Mechanism

It has been shown that the electromagnetic and weak forces of Nature are unified into one interaction known as the electroweak interaction [29]. Electroweak theory was pioneered by Abdus Salam, Sheldon Glashow, and Steven Weinberg in the 1970's [4–6] and experimentally verified by the discovery of the $W^{\pm}$ and Z bosons by the UA1 and UA2 collaborations at the Super Proton Synchrotron (SPS) of CERN in 1983 [30,31]. Without the introduction of the Higgs boson into this theory, there exist two resounding problems. First of all, the original theory alone is not renormalizable, meaning that it predicts unphysical values of scattering amplitudes for high energy scales. Furthermore, it does not explain why the photon and the other spin-1 bosons are not treated on the same footing: the photon is massless, whereas the $W^{\pm}$ and Z bosons are quite heavy, roughly 80 GeV and 91 GeV, respectively.

In order to resolve these two issues, we introduce the Higgs field, manifest in the

addition of a term to the Lagrangian of the electroweak interaction [25,26]. This Higgs field, a field mitigated by the Higgs boson and theorized to permeate all of space, couples to all particles (bosons and fermions) in proportion to their masses [15]. The act of the Higgs field giving mass to the fundamental particles through this coupling is known as the Higgs mechanism. Because it does not couple to photons, the photons remain massless. Thus, we see asymmetry between the photon and the $W^{\pm}$ and Z bosons in electroweak theory. This asymmetry is referred to as spontaneous electroweak symmetry breaking. To better illustrate the spontaneous nature of this symmetry breaking, let us first look at the general form of the Higgs field (ϕ) Lagrangian term discussed above:

$$\mathcal{L}_{Higgs} = \partial^{\mu}\phi\partial_{\mu}\phi - V(\phi), \tag{2.1}$$

where the first term is the kinetic contribution and the potential $V(\phi)$, illustrated in Figure 2-1, takes the form

$$V(\phi) = -a|\phi|^2 + b|\phi|^4. \tag{2.2}$$

Here, a and b are positive constants. A stable solution minimizing this term of the Lagrangian takes the form

$$\phi = \sqrt{\frac{a}{2b}}e^{i\theta}, \tag{2.3}$$

where θ is a real number between 0 and 2π. In order to reach a stable minimal state, the Higgs field must spontaneously pick some value of θ, breaking the U(1) symmetry of the system [25, 26]. The second issue mentioned above is now accounted for as well: the renormalizability of electroweak theory is upheld by the presence of the Higgs field due to the condition of local gauge invariance that it establishes [2,32,33].

The only remaining task at hand is to experimentally verify the Higgs mechanism through the discovery of the Higgs boson. This is particularly troublesome given that the Higgs boson mass is a free parameter of the theory. However, previous

experiments and theoretical considerations have narrowed the mass window of the Higgs boson mass to between roughly 110 GeV and 1000 GeV (where we have set $c = 1$) [20], which the LHC can completely explore. The lower bound is set by the results of the LEP experiment [34], while the upper bound is imposed by requiring unitarity of diboson scattering. Figure 2-2 illustrates some of the ways in which a Higgs boson can be produced from pp collisions at the LHC, while the various cross sections associated with Higgs boson production are presented as a function of Higgs boson mass in Figure 2-3.

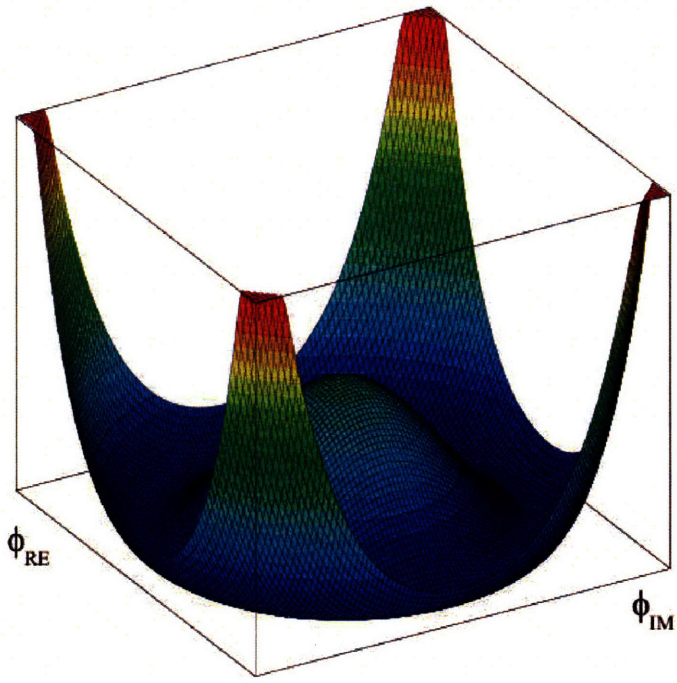

Figure 2-1: Illustration of the Higgs potential, $V(\phi)$. Because ϕ is complex-valued, there exists a ring of minima that correspond to possible ground states for the Higgs field. The spontaneous selection of this ground state breaks the symmetry of the system.

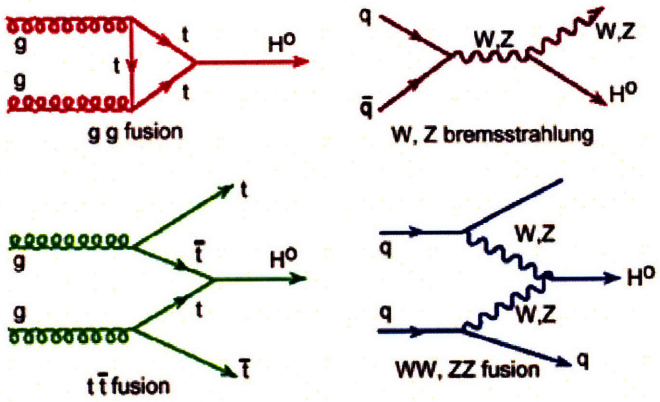

Figure 2-2: Feynman diagrams associated with four ways in which a Higgs boson can be produced from pp collisions. The interacting quarks and gluons are contained within the impinging protons. Note that all of the diagrams involve heavy particles because the strength of the coupling between the Higgs boson and other particles is proportional to the mass of the particle.

2.3 New Physics

Though the Standard Model, complete with Higgs boson, is one viable description of Nature, it leaves many questions unanswered. For instance, it does not explain the pattern of quark and lepton masses and mixing, why there are three generations of quarks and leptons, why neutrinos have such small masses, or provide an answer to the hierarchy problem [13]. Even how the $W^{\pm}$ and Z^0 bosons acquire mass is not solely explained by the existence of the Higgs boson. Therefore, many physicists are hopeful that new physics will be present at the energies of the LHC that could explain these open problems [18]. Current theories containing new physics include supersymmetry [7, 8], extra dimensions [9, 10], leptoquarks [11, 12], and small black holes [13, 14], among others. One of those most widely discussed theories is supersymmetry (SUSY), which relates elementary particles of one spin to another particle that differs by half a unit of spin. Supersymmetry thus relates fermions to bosons and vice versa, a connection that is not made by the SM and for which there is currently no direct experimental evidence [18, 20].

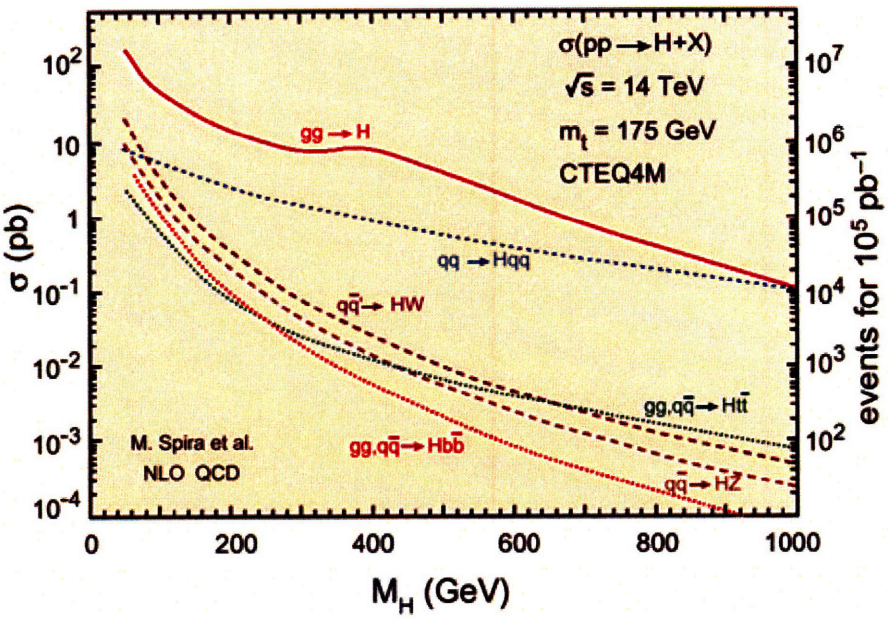

Figure 2-3: Cross sections associated with Higgs boson production from pp collisions as a function of Higgs boson mass, a free parameter in the Standard Model.

Chapter 3

Detector

Any Higgs bosons or other particles associated with new physics that are created in the proton-proton collisions of the LHC ultimately decay into a variety of hadrons, leptons, and photons (excluding exotic particles that have not yet been discovered) [18]. Thus, in order to reconstruct the original particles of interest, it is of primary importance to have the means to detect their decay products and measure their kinematic properties. The CMS detector is well-equipped in this regard. The detector contains a tracker, electromagnetic calorimeter, hadron calorimeter, and muon chambers, which collectively detect the presence of all of the above listed elementary particles except for neutrinos, which are reconstructed indirectly. In addition, the CMS detector contains between the hadron calorimeter and muon chambers a 4 T solenoidal magnet, which serves to bend charged particles, revealing their momentum and charge. Data collected from each beam collision in the various parts of the detector are filtered through a two-leveled trigger system before being transfered to the CMS Tier-0 processing center at CERN for analysis, reducing a massive 40 million beam crossings per second to a more manageable 100 recorded beam crossings per second [35]. This is necessary as most of the collisions are not interesting and there is not enough storage space to retain the information associated with every collision. An illustration

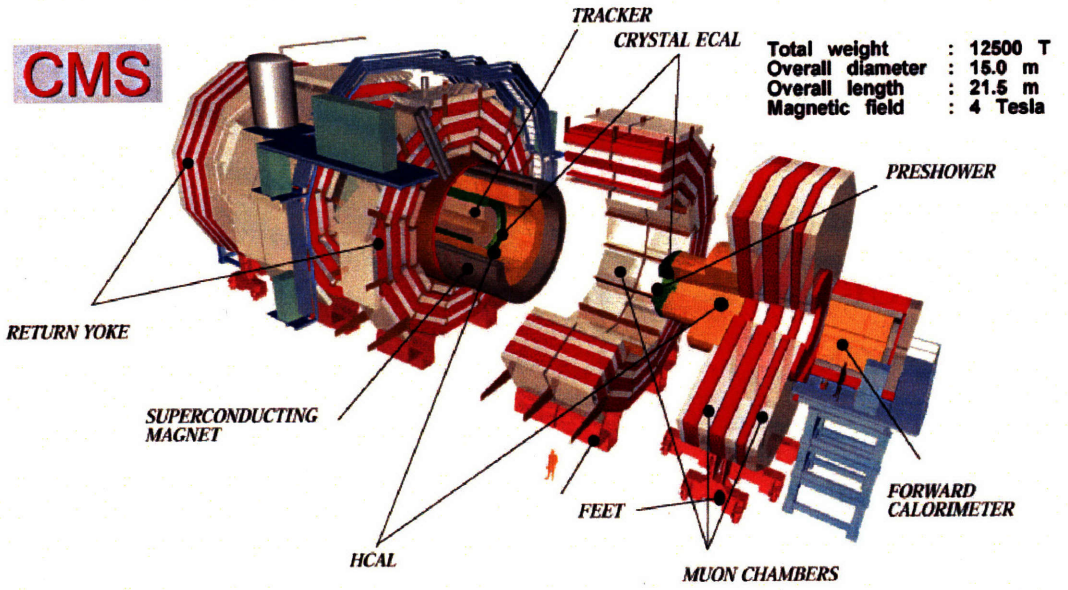

Figure 3-1: An overview of the CMS detector. In the middle, under the barrel, there is a man to give a sense of the scale (HCAL = hadron calorimeter, ECAL = electromagnetic calorimeter).

of the CMS detector as a whole is presented in Figure 3-1. Note that the detector is composed of a long barrel piece and two endcaps, making the detector hermetic with respect to particle flux.

Particle identification at a more incisive level is best accomplished by combining information available from different subsystems of the detector [20]. For example, electrons and photons both give energy deposits localized in the electromagnetic calorimeter, though the charged electron has an associated track in the tracker, whereas the neutral photon does not ionize and leaves no track (see Figure 3-2). Combining tracking and calorimetry therefore allows us to clearly distinguish between electrons and photons. Similar combinations of subsystem information elucidate the identity of hadrons and the other leptons. Neutral hadrons, such as neutrons, do not leave a track in the silicon tracker or deposit energy in the electromagnetic calorimeter, but lose most of its energy in the hadron calorimeter. Charged hadrons, such as charged pions and kaons, deposit a little energy in the electromagnetic calorimeter and quite a

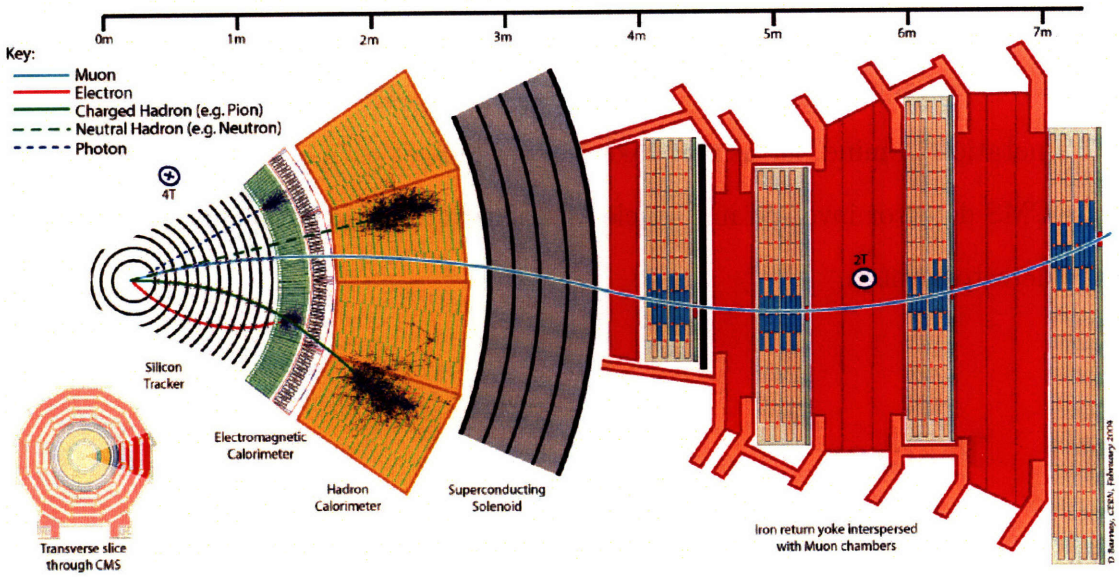

Figure 3-2: A transverse slice of the CMS detector.

bit of energy in the hadron calorimeter. Muons generally are the only detectable particles that make it to the muon chambers, the outermost detector subsystem, leaving very little energy in either of the calorimeters. Tau particles and the heavy hadrons and bosons decay before reaching the tracker and thus must be reconstructed using their decay products.

As for detector coordinate conventions [35], the CMS collaboration has defined the z-axis to point along the beam direction toward the Jura mountains, the azimuthal angle ϕ to be measured from the x-axis (which is parallel to the ground) in the x-y plane, and the polar angle θ to be measured from the z-axis. Pseudorapidity is, as usual, defined as $\eta = -\ln\tan(\theta/2)$ and is preferred over θ in hadron collider physics because particle production is constant as a function of pseudorapidity. The momentum and energy measured transverse to the beam direction, denoted by p_{T} and E_{T}, respectively, are computed from the x and y components. Ideally, the sum of E_{T} for all particles in the detector should be measured to be zero, since originally all of the energy in the collision is parallel to the beam. The imbalance of energy measured

in the transverse plane is denoted by $E_{\mathrm{T}}^{\mathrm{miss}}$, which is often attributed to either a bad measurement or the presence of neutrinos or other non-measurable particles. With this notation in mind, let us now take a closer look at each of the four main parts of the CMS detector involved in particle identification, working radially outwards from the detector center.

3.1 Tracker

The CMS tracker is located closest to the beam path in the center of the detector, with an inner radius of roughly 10 cm and an outer radius of nearly 110 cm. It is composed of finely segmented silicon pixels (66 million) and strips (9.6 million), enabling the measurement of the momentum and position of particles along its path through the extent of the tracker [36]. By considering the charged particle flux at various radii at high luminosity, three distinctive regions are delineated [35]. Closest to the interaction vertex where the particle flux is highest (10 cm $< r <$ 20 cm), pixel detectors are placed. Having these pixel detectors with high spatial resolution very close to the beam allows for the precise measurement of particle interaction vertices from pp collisions. In the intermediate region (20 cm $< r <$ 55 cm) and outer region (r $>$ 55 cm), the particle flux is low enough to enable use of silicon microstrip detectors (smaller ones for the intermediate region and larger ones for the outer region). These detectors have less spatial precision and have significant combinatorial background in a very high particle flux environment. They are used primarily to measure the momentum associated with particle tracks [36].

As only charged particles can lead to ionization in the tracker and thus the presence of a track, the tracker plays an important role in distinguishing between electrons and photons [36]. This is of particular importance to our analysis as possible electron misidentification could be the result of a missing electron track, leading to the

erroneous detection of a photon. The tracker pixel detectors have a pitch, or separation between detection elements, of roughly 100 μm. Because of this, it is possible for the tracker to identify particles with a separation between primary vertex (where the particle is formed) and secondary vertex (where the particle decays) that exceeds 50 to 100 μm with both vertices lying within the tracker. Such particles include τ leptons and hadrons containing c or b quarks.

3.2 Electromagnetic Calorimeter

The next section of the CMS detector is the electromagnetic calorimeter (ECAL). The ECAL is a hermetic, homogeneous calorimeter containing 61,200 lead tungstate ($PbWO_4$) crystals mounted in the central barrel part that is closed by 7,324 crystals in each of the two endcaps [37]. Lead tungstate scintillating crystals were chosen for the electromagnetic calorimeter of CMS because they are fast and have short radiation lengths ($\sim$90 cm) leading to more contained electromagnetic showers [35]. Photodetectors (silicon avalanche photodiodes in the barrel and vacuum phototriodes in the endcaps) that operate well in magnetic fields are used to compensate for the relatively low light yield of the crystals. The crystals are organized into 5 by 5 crystal blocks known as superclusters, or alternatively, calo-towers [35]. Energy deposited by showering particles is collected in these calo-towers, reconstructing the energy of the original incident particle.

The two basic radiative processes responsible for the creation of electromagnetic showers in the calorimeter are Bremsstrahlung by the electrons and electron-positron pair production by the photons. Once the shower multiplication process begins producing particles with energies too low to participate in radiative processes, the particles in the shower lose energy by interacting with the crystals and eventually come to rest [20]. There is a characteristic length scale for radiative processes in the ma-

terial of the calorimeter called the radiation length, X_0. Electromagnetic showers in calorimeters typically run their courses in about twenty radiation lengths, while the characteristic transverse size of the shower is roughly one radiation length [20]. This indicates that photons and electrons can be well-localized transverse to the point of impact on the calorimeter by the calorimetric measurement. Therefore, the calorimetric technique measures both energy and position, although the position measurement is crude compared to tracking data.

As mentioned above, the electromagnetic calorimeter plays a major role in the detection of photons and electrons. This is crucial to our analysis of $ZZ \rightarrow 4\ell$, because we must be able to effectively detect electrons and understand their misidentification. In addition, the CMS electromagnetic calorimeter plays a significant role in measuring the energy of quark and gluon jets as well as missing transverse energy due to neutrinos and other non-measurable particles [37].

3.3 Hadron Calorimeter

The CMS hadron calorimeter serves an analogous purpose to the electromagnetic calorimeter in that it is chiefly useful in measuring particle energy, and to a lesser extent, particle position. However, the hadron calorimeter (HCAL) is much more useful for detecting quark and gluon jets that give rise to hadrons as opposed to electrons or photons [35]. These jets result from highly energetic quarks and gluons (from the initial proton-proton collision or immediate decays) that continuously produce quark-antiquark pairs and strings of gluons [20]. Eventually, as particle energy diminishes with increasing particle number, hadronization ensues, resulting in the formation of hadrons. These hadrons (and their decay products, if any) are then detected, and the total jet energy (from the original quarks and gluons) is measured. Due to the large number of intermediate states, the direction (and position) of the parent quark

or gluon is poorly measured through the calorimetric jet measurement. The HCAL is composed of layers of brass interleaved with plastic scintillators. The geometry is chosen such that the brass layers overlap, creating hermetic layers of highly absorbent material without cracks [35].

3.4 Muon Chambers

The outermost layers of the CMS detector consist of the muon chambers, which are distributed within an iron return yoke assembly used to provide a magnetic field opposite in direction to that within the solenoid. The muon chambers are composed of three different types of gaseous detectors: drift tube chambers, cathode strip chambers, and resistive plate chambers [35]. The drift tube chambers are located in the barrel of the detector, the cathode strip chambers are located in the detector endcaps, and the resistive plate chambers are located in both. These gaseous muon chambers work together with the tracker to determine the momentum of each incident muon. The drift tube chambers and the cathode strip chambers have very good spatial resolutions (50 to 100 μm [35]) and are primarily used for tracking. The resistive plate chambers have a much better temporal resolution (1 to 2 ns) and are used to correct tracking ambiguities [38].

As the muon mass is much larger than the electron mass, they lose relatively little energy from Bremsstrahlung radiation in the tracker and calorimeters [38]. This, in addition to the relatively long decay length of the muon and the relatively short decay length of most other particles present in the detector, results in muons being the most prevalent particle by far on relative terms within the CMS muon chambers. Additionally, muons have a fake rate that is typically an order of magnitude or more lower than the fake rate for electrons [39]. Muon-based analyses are thus very clean with relatively little associated background. However, statistical limitations still pose

problems for muon-based analyses [18, 35].

Chapter 4

Electron Identification

Electron identification is generally split into two separate analyses: the calculation of electron efficiencies and the calculation of electron fake rates. The former calculation determines the fraction of real electrons that were correctly reconstructed while the latter one illuminates the fraction of reconstructed electrons that were incorrectly reconstructed. These analyses are prerequisites to a cross section measurement, including associated statistical and systematic uncertainties, of many Higgs decay channels. Electron efficiency analysis from single boson decays, which generally have much larger cross sections than diboson decays, are used to help reduce systematic uncertainty on diboson cross sections due to less uncertainty on the efficiency (resulting from more statistics). Electron fake rate analysis is used to correct the background to signals of interest, yielding higher discovery potentials from a reduction in background counts. We apply the results of these two studies to the $ZZ \rightarrow 4\ell$ decay channel in the next section. Additionally, later in this section we study the result of cut relaxation on calculated electron efficiencies and fake rates.

4.1 Electron Efficiency

Our first study concerning electron identification involves the determination of the ratio of correctly identified electrons over the total number of electrons passing through the detector. This number is referred to as the efficiency of electron detection. The electron efficiency is a parameter in the calculation of cross section, allowing us to translate the number of electrons identified per unit of integrated luminosity into the total number of electrons per unit of integrated luminosity. It is therefore necessary to accurately determine the electron efficiency using generator-level information from Monte Carlo studies. We also develop reconstruction-level methods to be used to determine the electron efficiency from data once the LHC beam starts up. Additionally, a study on charge misidentification in the sample is discussed.

4.1.1 Sample

For our electron efficiency analysis, we make use of $Z \rightarrow 2e$ (one electron, one positron) full simulated samples generated using version 1.3 of the CMS simulation, reconstruction, and analysis software package (CMSSW). The $Z \rightarrow 2e$ channel is used as it is not unreasonable to assume that electrons can be identified independently with uncorrelated efficiencies, which would allow these efficiencies to be used in the $ZZ \rightarrow 4e$ sample. Then we can make use of the much larger number of $Z \rightarrow 2e$ events in order to compute electron efficiencies for $ZZ \rightarrow 4e$ with lower associated statistical uncertainty.

4.1.2 Efficiencies

We split the electron efficiency study into two parts: one using generator-level information from Monte Carlo simulations and the other using reconstruction-level techniques that can be used once the LHC begins delivering pp collisions. The latter part of the study has much more use in practice as the Monte Carlo simulations will

likely not fully represent the data samples. However, analysis using the Monte Carlo simulations has much use as well as it allows us to avoid introducing bias into our efficiencies.

4.1.2.1 Using Monte Carlo Simulations

We begin by determining electron efficiency in the CMS detector using generator-level information. This requires checking the number of particles reconstructed in the detector that pass electron identification cuts and dividing it by the total number of generated electrons that pass through the detector. The electron identification cuts include several kinematic cuts. Setting $c = 1$, we require that $E_{\mathrm{T}} > 7$ GeV, $|\eta| < 2.5$, $E/p > 0.8$, $1/E - 1/p < 0.06$ GeV^{-1}, $E_{\mathrm{HCAL}}/E_{\mathrm{ECAL}} < 0.05$, where E_{HCAL} is the total energy detected in the HCAL and E_{ECAL} is the total energy detected in the ECAL, and $d_0 < 0.01$ cm, where d_0 is the track impact parameter. We refer to all particles that pass these kinematic cuts as "reconstructed electrons". The first two of these cuts are fiducial cuts, selecting particles in a range of E_{T} and η in which the CMS detector performs well. The next three cuts select particles that deposit little energy in the tracker and very little energy in the HCAL, instead losing most of their energy in the ECAL. This type of energy deposition pattern is indicative of a electron passing through the detector.

Besides the basic kinematic cuts, we require two isolation cuts: $I_{\mathrm{track}}/E_{\mathrm{T}} < 0.2$ and $I_{\mathrm{calo}} < 15$ GeV, where I_{track} is the total energy of surrounding tracks in the tracker and I_{calo} is the total energy collected outside of the primary supercluster in the ECAL. We refer to all particles that pass these isolation cuts, in addition to the previous kinematic cuts, as "identified electrons". These cuts reject quark and gluon jets, which are very broad in extent. A summary of the kinematic and isolation cuts for identified electrons is given in Table 4.1. The electron efficiency is parameterized in terms of generator-level information and is presented in Figure 4-1. The total

electron efficiency is calculated to be about $75\% \pm 1.2\%$. It is important to note that the "dips" in the η distribution around ± 1.5 are due to overlap between the barrel and endcap detector pieces, leading to a reduced efficiency in electron reconstruction. The detector's ability to successfully reconstruct particles drops for large values of $|\eta|$, leading to a drop-off in electron efficiency.

Cut Parameter	Cut Value
E_{T}	> 7 GeV
$\lvert\eta\rvert$	< 2.5
E/p	> 0.8
$1/E - 1/p$	< 0.06 GeV^{-1}
$E_{\mathrm{HCAL}}/E_{\mathrm{ECAL}}$	< 0.05
d_0	< 0.01 cm
$I_{\mathrm{track}}/E_{\mathrm{T}}$	< 0.2
I_{calo}	< 15 GeV

Table 4.1: Identified electron kinematic and isolation selection criteria.

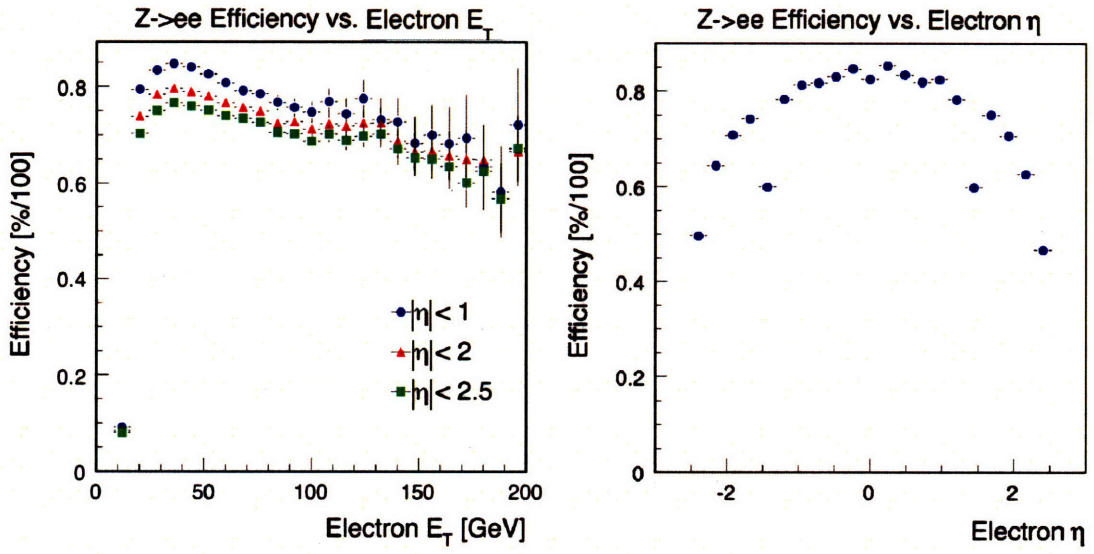

Figure 4-1: Z→2e electron efficiencies derived from Monte Carlo samples, parameterized in terms of E_{T} (left) and η (right) of the electron. Note that the efficiency distribution is relatively flat for large E_{T} and for small $|\eta|$.

4.1.2.2 Using Data

While it is informative to calculate electron efficiencies using generator-level information, it is much more useful to be able to calculate them from data. Without generator-level information, we must turn to using generic reconstruction objects as potential candidates for electron identification. Both tracks and calo-towers are acceptable reconstruction objects for this job, a priori. Further analysis (see Figure 4-2) shows that using tracks is not a good idea because the total reconstructed Z mass from a track candidate plus the original tagged electron is not representative of the reconstructed Z mass from the actual two electrons. Much better agreement is found by using calo-towers, and so we use them as our generic reconstruction objects.

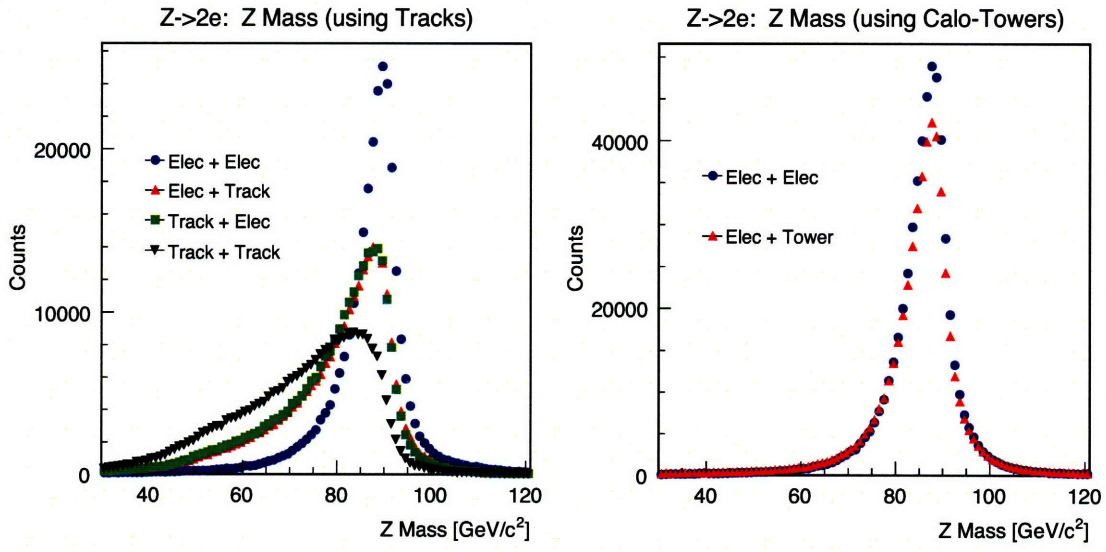

Figure 4-2: Reconstructed Z masses using tracks (left) and calo-towers (right) as generic reconstruction objects for $Z \rightarrow 2e$ data-like electron efficiency calculation. The plots compare the Z mass using combinations of reconstructed electrons, matched tracks, and matched calo-towers.

The reconstruction-level technique that we employ involves first tagging one good reconstructed electron and then matching a reconstructed calo-tower to it. This

reconstructed calo-tower must satisfy $E_T > 7$ GeV, $|\eta| < 2.5$, and $\Delta\phi > 10°$, where $\Delta\phi$ is the difference in ϕ between the tagged electron and the calo-tower. The first two cuts are applied for the same reason as for electrons, as this is the regime of parameter space where the detector performs well. The cut on $\Delta\phi$ prevents the matching algorithm from picking a calo-tower that corresponds to the tagged electron and additionally serves as an isolation cut. Of the calo-towers that satisfy these requirements, we pick the one with the highest E_T because it is most likely to match to a $Z \rightarrow 2e$ electron. To correctly account for all of the energy of the second electron, which we refer to as the "probe" electron (as it is our probe of electron efficiency), we must add up the energy of surrounding calo-towers in the ECAL to the original calo-tower. Doing so leads to the construction of another object, which we refer to as a calo-tower-sum. Another cut is made on the calo-tower-sum, requiring the reconstructed Z mass from the combination of the tagged electron and calo-tower-sum to be between 75 GeV/c^2 and 105 GeV/c^2.

We next match this calo-tower-sum to another reconstructed electron, the probe electron, if one exists close to the calo-tower-sum. The ratio of the number of cases where there is a match to a probe electron to the total number of cases considered, as in, reaching the calo-tower-sum stage, yields the data-like electron efficiency. By matching the calo-tower-sum to a generator-level electron and then matching that electron to a reconstructed electron, we can also calculate a generator-level electron efficiency using this method. We find a generator-level electron efficiency of $77.5\% \pm 1.3\%$ and a data-like electron efficiency of $77.0\% \pm 1.3\%$. The similarity of the two values and associated E_T distributions, as illustrated in Figure 4-3, shows that the efficiency calculations are consistent. The data-like electron efficiency calculated and parameterized here is used in the $ZZ \rightarrow 4\ell$ cross section measurement that we perform in the next chapter.

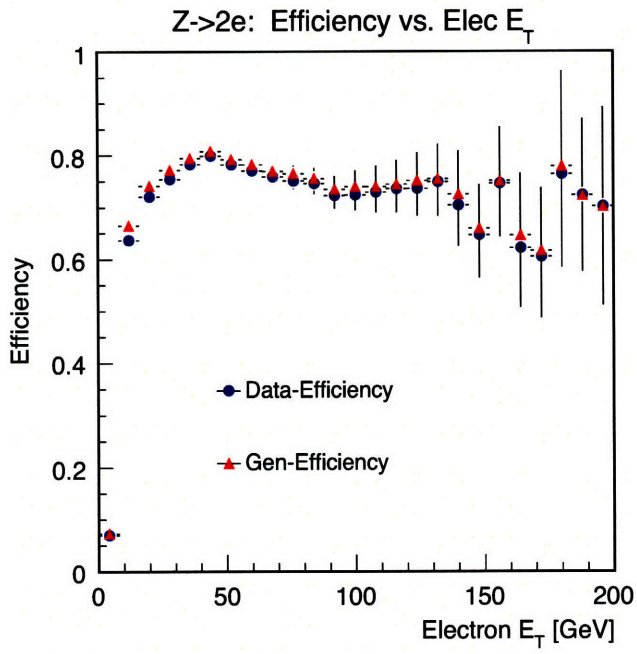

Figure 4-3: Electron efficiencies as a function of E_T from matching calo-tower-sums to good reconstructed electrons ("data-efficiency") and from matching generated electrons (already matched to calo-tower-sums) to good reconstructed electrons ("gen-efficiency"). There is excellent agreement between the two distributions.

4.1.3 Charge Misidentification

Another brief study we perform using the $Z \rightarrow 2e$ Monte Carlo samples is the determination of the fraction of reconstructed e^+e^- pairs with one of the electrons or positrons incorrectly reconstructed in terms of its charge. In Figure 4-4, we show the relative abundance of correctly reconstructed e^+e^- pairs compared to incorrectly reconstructed e^+e^- pairs, illustrated using the reconstructed Z mass. We calculate an overall electron pair charge misidentification rate of $3.0\% \pm 0.3\%$, meaning that roughly 3% of the electron pairs have at least one electron with incorrectly assigned charge upon reconstruction. This implies an approximate charge misidentification rate of $1.5\% \pm 0.2\%$ for individual electrons/positrons. Misidentification of charge most likely is the result of a poorly reconstructed track that misleadingly appears to

bend in the opposite direction in the magnetic field of the detector. However, as Figure 4-4 upholds, the charge misidentification still gives rise to a correct reconstructed Z mass distribution.

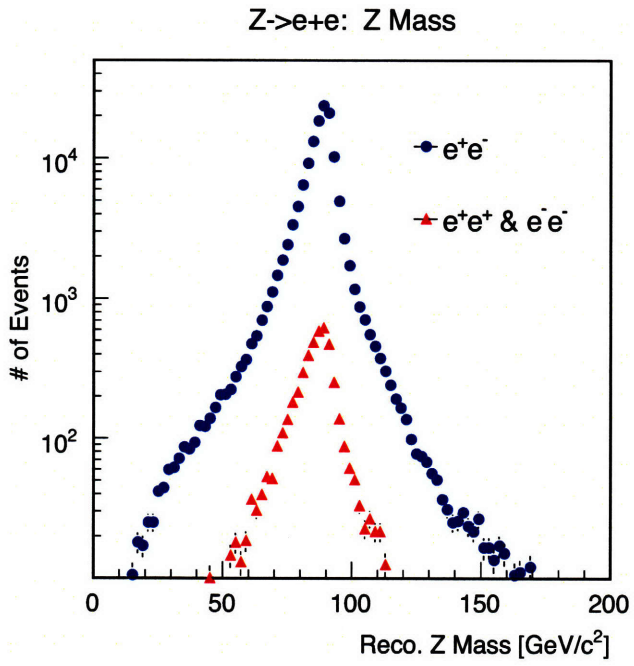

Figure 4-4: Reconstructed Z masses corresponding to correctly reconstructed e^+e^- pairs (shown in blue) and incorrectly reconstructed e^+e^+ or e^-e^- pairs (shown in red).

4.2 Electron Fake Rate

Our next analysis concerning electron identification involves the determination of the rate at which the detector misidentifies a non-electron particle, such as a photon, as an electron. This is known as the electron fake rate within the detector. Much like the electron efficiency, its value must necessarily be between 0 and 1. A fake rate of 0% means that all reconstructed electrons are real electrons and a fake rate of 100% corresponds to all reconstructed electrons being misidentified electrons. We

study the electron fake rate in order to get a handle on systematics and to correct the background to $ZZ \rightarrow 4\ell$ signal with the aim of improving the discovery potential of the channel, because the correction reduces the total background. In addition, we identify the faking particles and analyze the content of the jets responsible for causing the electron fakes. It is important to note that fake rate studies are more difficult to perform than efficiency studies, as in principle many different types of particles can fake electrons. Isolating pure Monte Carlo samples of each possible faking particle or set of particles and properly weighting them to find the correct fake rate is very difficult. Furthermore, fake particle reconstruction is not expected to be very accurate using the Monte Carlo simulations, and so ultimately data must be used. Because the electron fake rate and $ZZ \rightarrow 4\ell$ background that we find are very small, we only focus on two high cross section channels that are likely to be the main contributors using Monte Carlo simulations.

4.2.1 Samples

The majority of electron-faking particles within the detector, according to Monte Carlo results, are either photons or hadrons from quark and gluon jets [18]. Therefore, in our fake rate analysis we must focus primarily on high cross section samples featuring photons and jets as final-state particles. Two important channels satisfying these requirements are: the QCD Compton effect, $qg \rightarrow \gamma q$, which we refer to as the photon jet channel, and any process involving strictly quark and gluon jets, referred to as the QCD channel. These processes can be generalized to $ZZ \rightarrow 4\ell$ background channels based on the particular final-state of each channel. In our analysis, we make use of fully simulated photon jet and QCD samples generated using version 1.3 of CMSSW.

4.2.2 Fake Rates

In our fake rate analysis, we apply slightly different cuts to the photon jet and QCD samples. For the photon jet samples, we first require presence of the $\gamma + q$ reconstructed final-state. This includes the presence of one reconstructed photon with $E_T > 20$ GeV and $|\eta| < 2.5$ as well as at least one reconstructed jet with $E_{\mathrm{T}} > 25$ GeV and $|\eta| < 2.0$. Both the photon and the jet must also satisfy a few other kinematic and isolation cuts similar to those for a reconstructed electron. Note that the jet has looser isolation cuts due to generally being very broad in extent. Next, we require that $\Delta\phi$ between the reconstructed photon and jet be at least 160°. To calculate the electron fake rate, we divide the number of events that meet these requirements and contain a reconstructed electron near the reconstructed jet by the total number of events that pass the cuts but do not have a reconstructed electron near the reconstructed jet. Thus, only events that have the possibility of faking an electron are considered in the calculation of electron fake rate. Parameterized photon jet fake rate distributions are shown in Figure 4-5. We find an overall photon jet fake rate of $(1.7 \pm 0.5) \cdot 10^{-3}$.

For the QCD samples, we apply two different sets of cuts for comparison. We use two separate sets of cuts in order to check if the fake rate changes based on the selection of either one or two jets. The first set of cuts, which we refer to as "QCD 1", involves selecting the highest E_{T} jet satisfying $E_{\mathrm{T}} > 25$ GeV and $|\eta| < 2.0$. The electron fake rate is then determined by finding the fraction of these events where there is a good reconstructed electron near the reconstructed jet. The other set of cuts, which we refer to as "QCD 2", involves selecting the two highest E_{T} jets in the event with the highest E_{T} jet satisfying $E_{\mathrm{T}} > 25$ GeV and $|\eta| < 2.0$. The second highest E_{T} event must satisfy $E_{\mathrm{T}} > 15$ GeV and $|\eta| < 2.0$. In this case, the electron fake rate is determined by finding the fraction of these events where there is a good reconstructed electron near one of these two reconstructed jets. Our fake rate analysis

results are displayed in Figure 4-5. Note that the two sets of QCD cuts produce very similar efficiency distributions. We find an overall QCD fake rate of $(0.6 \pm 0.2) \cdot 10^{-3}$, which is almost a factor of three lower than the corresponding fake rate for the photon jet samples.

These fake rate distributions can be applied to the $ZZ \rightarrow 4\ell$ background channels. Due to having extremely little background, it turns out that we need not apply these fake rates in our analysis. This is discussed in more depth when we later discuss the calculation of $ZZ \rightarrow 4\ell$ cross sections. We must be careful to note that the fake rates are dependent on instantaneous luminosity and will increase during the operation of the LHC due to pile-up and other considerations.

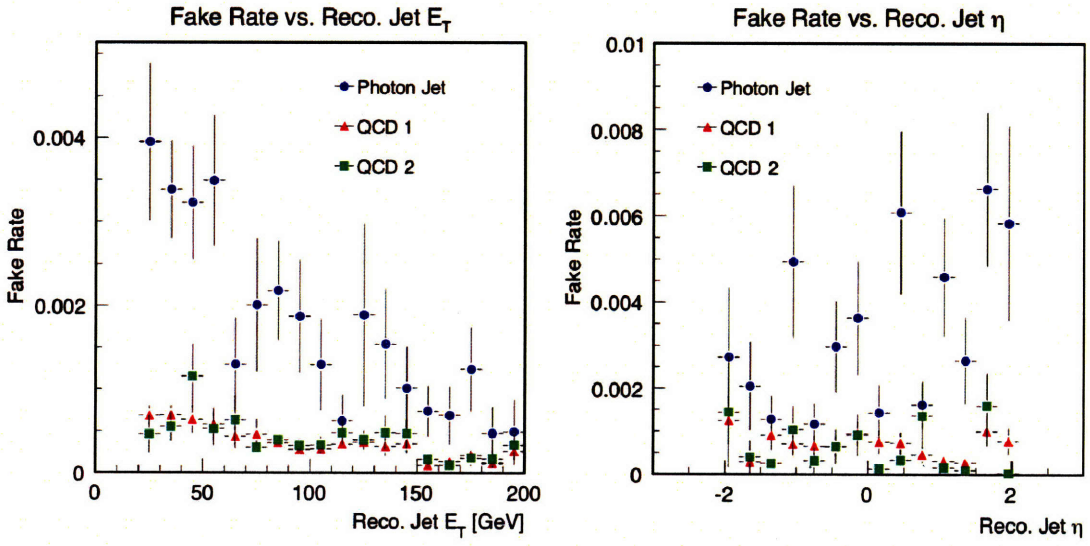

Figure 4-5: Fake rates for photon jet and QCD samples parameterized in jet E_{T} (left) and η (right). The η distributions are flat as expected [18].

4.2.3 Faking Particles

The next step of our analysis takes a closer look at the particular particles involved in faking reconstructed electrons within the detector. In our analysis, each "fake" event contains a reconstructed jet very close to a reconstructed electron. While many of these fakes are due to a hadron in the jet, such as a pion or kaon, often there are other causes for the reconstruction of a non-existent electron, including a photon produced in Bremsstrahlung or even a real electron or positron from pair-production or hadron decays. It is interesting to determine the identity of the faking particles in both the photon jet and QCD samples. However, since we have limited generator-level information for the QCD samples, we can only do this for the photon jet channel.

In order to obtain a firmer grasp on the identities of faking particles in our photon jet samples, we do the following. First, we loop through all generator-level particles and select the ones that are close to the jet that fakes an electron, with $\Delta R \equiv \sqrt{(\Delta\eta)^2 + (\Delta\phi)^2} < 0.2$ with respect to the jet center. Then, we loop through these particles and look for a generator-level particle with a value of E_T that is within 30% of the E_{T} of the reconstructed electron. We pick the faking particle based on an ordered list, in case more than one type of particle falls within this group of generator-level particles: precedence is given to real electrons/positrons, then pions/kaons, photons, and finally "others". If no generator-level particles fall within 33% of the E_{T} of the reconstructed electron, we pick the generator-level particle with the highest value of E_{T}. Further analysis suggests that there are very few cases where there is not exactly one clear electron-faking particle candidate.

Our results are shown in Figure 4-6. The majority of the electron-faking particles are pions, though kaons and photons play a large role at medium energies and real electrons/positrons at lower energies.

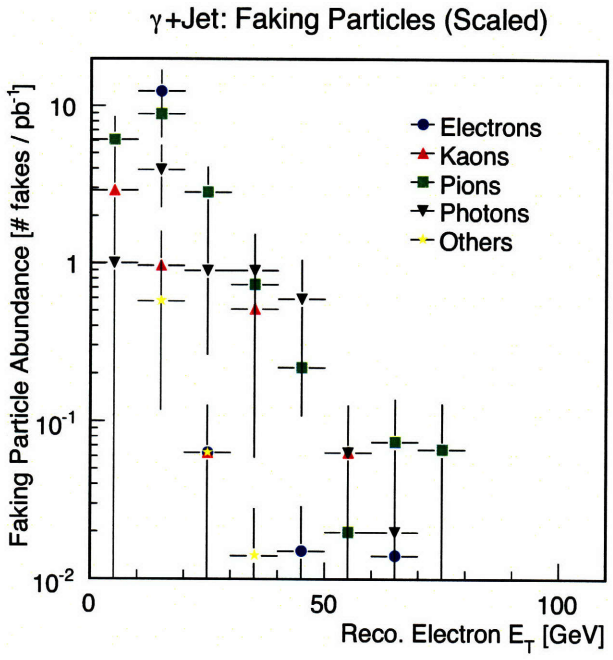

Figure 4-6: Electron-faking particle identification for the photon jet channel. Note that the above electrons (blue) are real electrons/positrons produced from the interaction of jets and/or photons with the detector.

4.2.4 Jet Content

Another study in our analysis of much interest is the determination of the content of faking jets, or more specifically, the dominant particle type present in the faking jet of the photon jet samples. This includes $u/d/s$ quarks which we lump together, c quarks, b quarks, and gluons. We only look at the photon jet samples due to the limited generator-level information that we have for the QCD samples. In order to determine the jet content, we must use generator-level information to probe the interaction vertex and find what particle is the "mother" of the first photon generated in the event (meaning, the particle that gave rise to the photon). This particle in turn should be representative of the jet content in the faking jet of that event, as the photon and the jet that fakes an electron should have the same mother due to both

being produced from the same QCD Compton effect interaction.

Figure 4-7 illustrates the results of this analysis. It appears that the b quark jets have a much higher fake rate than the other quark jets and gluon jets, over many different values of E_{T}. We find a fake rate of $(1.7\pm0.7)\cdot10^{-2}$ for the b quark jets, which is about an order of magnitude higher than the previously determined overall photon jet fake rate of $(1.7 \pm 0.5) \cdot 10^{-3}$. Because of an especially high fake rate dominant at lower values of E_{T}, it is reasonable to associate the real electrons/positrons of our faking particle identification study with semi-leptonic decays of hadrons.

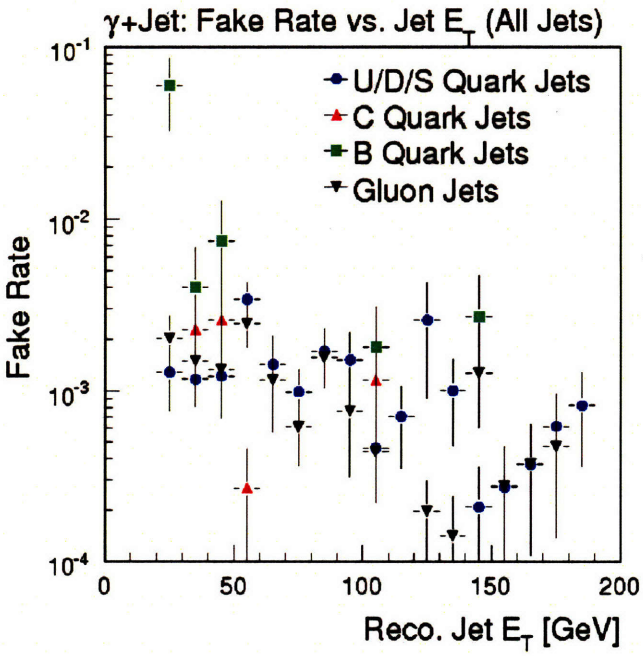

Figure 4-7: Fake rate of electron-faking jets of different quark/gluon content within the photon jet samples. The b quark jets have a much larger fake rate than the other jet types.

4.3 Cut Relaxation

Having computed both electron efficiencies and fake rates, we consider another study involving relaxing particular cuts for reconstructed electrons. In this study, we take out all isolation cuts and all kinematic cuts except for $E_{\mathrm{T}} > 7$ GeV and $|\eta| < 2.5$. We now refer to this as "electron reconstruction" and the inclusion of all cuts as "electron identification". Figure 4-8 illustrates the results of this cut relaxation analysis. As expected, both electron efficiency and fake rate increases as a result of the cut relaxation. Optimization in this regard could be particularly helpful in improving signal to background ratios, though we do not present such a detailed analysis here. Because of the small amount of background that we find below for $ZZ \rightarrow 4\ell$, it is likely that loosening the cuts would be beneficial as the improvement in efficiency would increase the signal significance while the increase in fake rate would have a negligible effect.

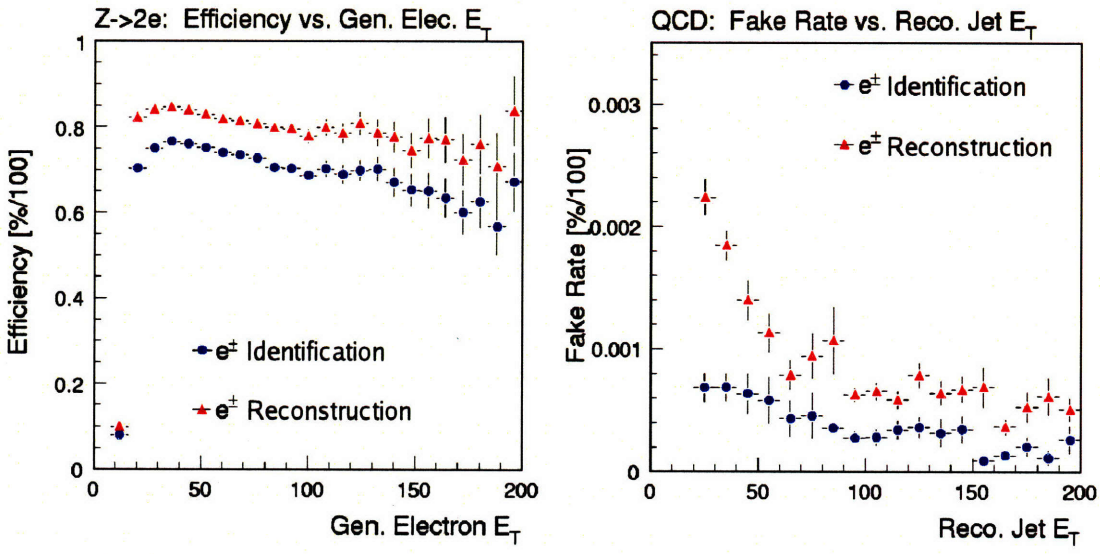

Figure 4-8: Result of cut relaxation analysis on electron efficiency (left) and electron fake rate (right). Both increase as a result of the cut relaxation. Note that "identification" includes all cuts, while "reconstruction" only uses minimal kinematic cuts, as described in the text.

Chapter 5

$ZZ \rightarrow 4\ell(e, \mu)$ Cross Section

Finally, we perform a calculation of the cross sections associated with the $ZZ \rightarrow 4\ell(e, \mu)$ channels, incorporating electron efficiencies and fake rates found in the previous chapter and previously calculated muon efficiencies and fake rates [39]. This calculation involves signal versus background optimization, which we perform first. The $H \rightarrow ZZ \rightarrow 4\ell$ Higgs decay channel is a very important channel for Higgs discovery because its branching ratio is quite large over a wide range of values for the Higgs mass, as seen in Figure 5-1. It is especially large for $m_H > 150$ GeV/c^2 and is the key channel in the Higgs discovery. Though $ZZ \rightarrow 4\ell$ is normally a background to $H \rightarrow ZZ \rightarrow 4\ell$, we treat the former as signal in order to develop reconstruction-level techniques for performing signal vs. background optimization and cross section calculation. This paper focuses on electron identification but we incorporate results of similar muon identification studies in our complete analysis of $ZZ \rightarrow 4\ell(e, \mu)$ [39].

5.1 Samples

In this section, we will treat a few different signals against a variety of backgrounds present due to the complexity of the proton-proton collisions. All Monte Carlo samples discussed here are fully simulated samples generated using version 1.3 of CMSSW.

5.1.1 Signal

Our analysis of $ZZ \rightarrow 4\ell(e, \mu)$ consists of three different signal channels that we consider separately. These channels are $ZZ \rightarrow 4e$ (two electrons, two positrons), $ZZ \rightarrow 4\mu$ (two muons, two antimuons), and $ZZ \rightarrow 2e2\mu$ (one electron, one positron, one muon, one antimuon). All three channels are present in the same $ZZ \rightarrow 4\ell$ Monte Carlo sample, in which Z bosons are forced to decay into leptons. An example of a $ZZ \rightarrow 4e$ event in the CMS detector is shown in Figure 5-2, and a $ZZ \rightarrow 4\mu$ event in Figure 5-3. Note that these samples include intermediate tau particles that decay into electrons or muons, though almost all of these events are eliminated through our cuts.

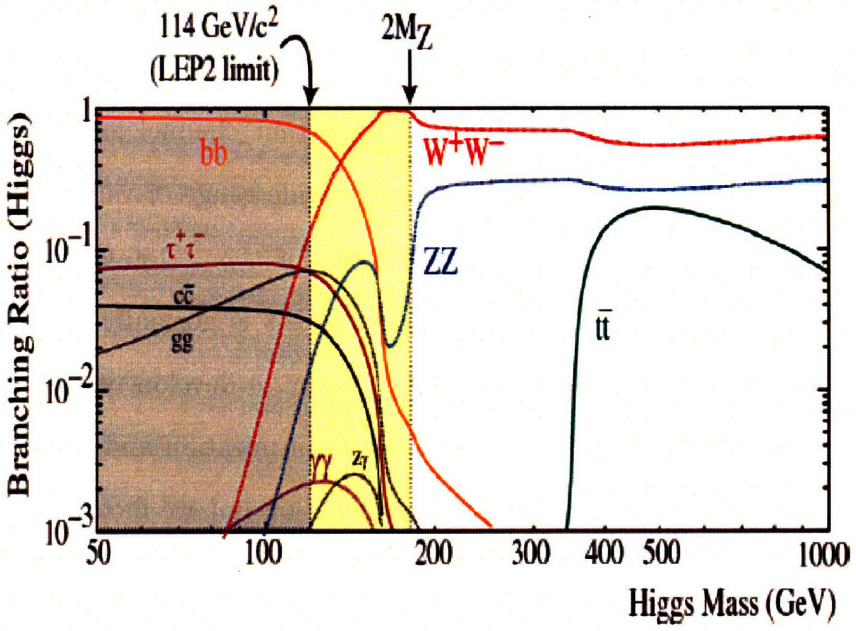

Figure 5-1: Various branching ratios of Higgs decay channels. Note that the ZZ decay channel has a large branching ratio for a wide range of values for the Higgs mass.

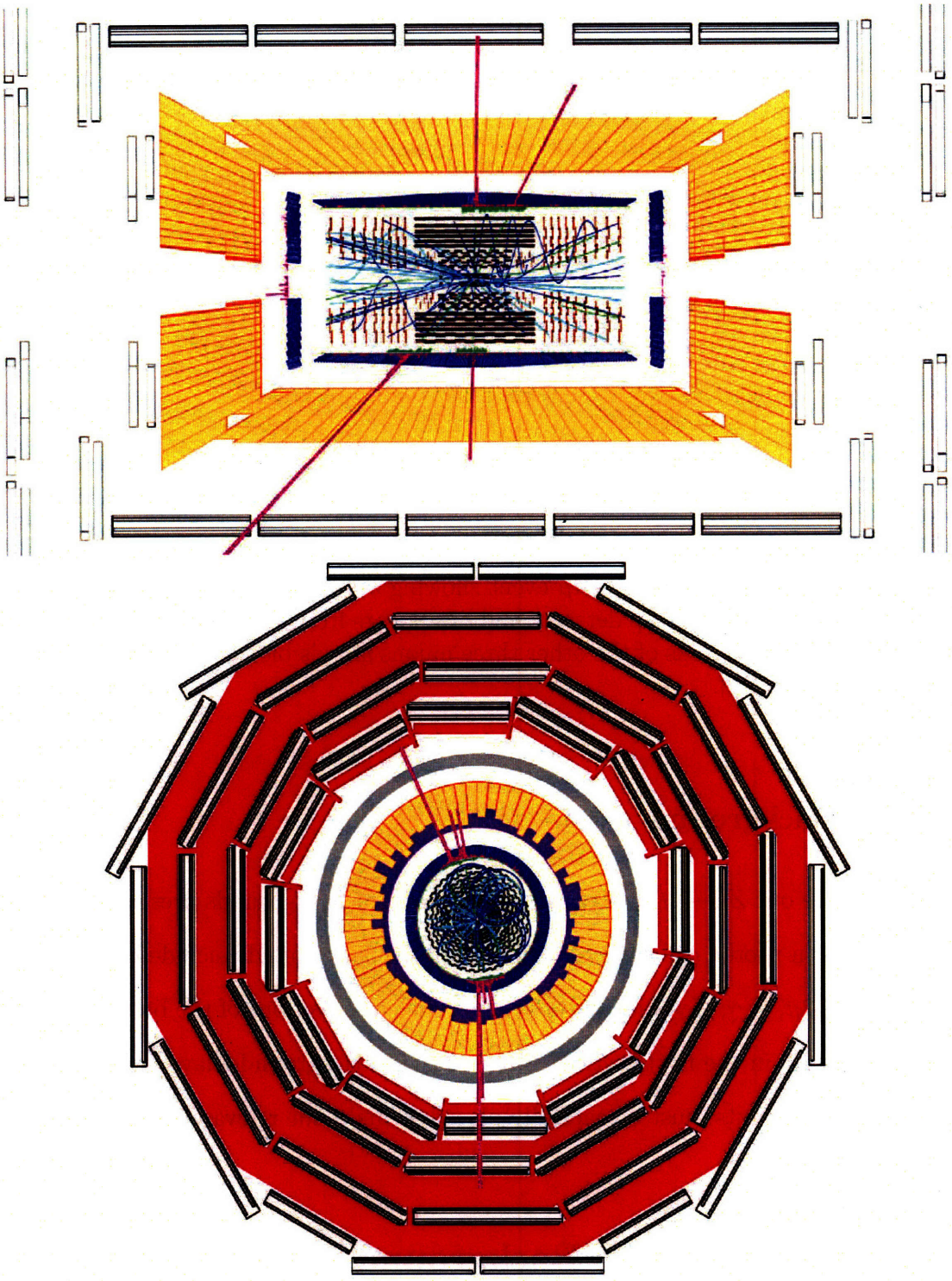

Figure 5-2: Display of an event candidate in the CMS detector for $ZZ \rightarrow 4e$. The event is shown in a longitudinal (top) and transversal (bottom) projection of the detector. Clearly visible are the four electrons as large energetic entries in the electromagnetic calorimeter [18].

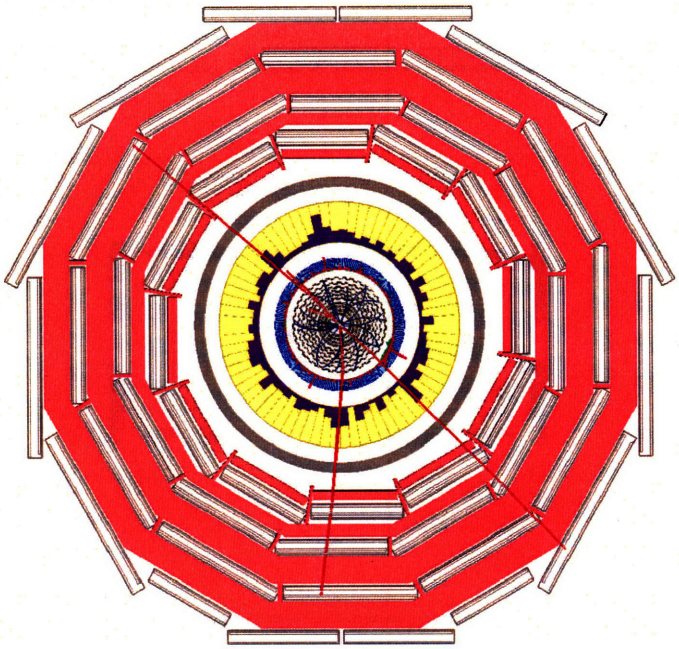

Figure 5-3: Example of a $ZZ \rightarrow 4\mu$ event showing only the reconstructed tracks. One muon travels into an endcap detector and disappears from this transversal projection. The reconstructed tracks of the other three muons are visible here, extending into the muon chambers [18].

5.1.2 Background

We complete our $ZZ \rightarrow 4\ell$ analysis using a variety of backgrounds present in the high energy proton-proton collisions of the LHC. These backgrounds include WZ, WW, $t\bar{t}$, $Z \rightarrow 2e$, $Z \rightarrow 2\mu$, $W\gamma$, $Z\gamma \rightarrow 2e$, and $Z\gamma \rightarrow 2\mu$. The cross sections of the backgrounds are listed in tables in the next section. Some of these backgrounds have very large cross sections, and so cuts must be carefully placed to make the relevant signal detectable.

5.2 Signal Versus Background Optimization

In our analysis, we perform signal versus background optimization using slightly different cuts depending on the signal channel. Most of the cuts that we perform for electrons are simply the cuts described in our electron identification analysis above,

namely the kinematic and isolation cuts that define an identified electron (see Table 4.1). Likewise, an "identified muon" has an analogous set of kinematic and isolation cuts. The kinematic cuts require $E_T > 7$ GeV, $|\eta| < 2.5$, $p_{T,Err}/p_T < 0.2$ (where $p_{T,Err}$ refers to the uncertainty on the value of p_T determined by the tracker), and $d_0 < 0.1$ cm. The muon isolation cuts require $I_{track} < 10$ GeV, $I_{track}/p_T < 0.2$, and $I_{calo} < 5$ GeV [39]. A summary of the kinematic and isolation cuts for identified muons is presented in Table 5.1.

Cut Parameter	Cut Value
E_T	> 7 GeV
$\|\eta\|$	< 2.5
$p_{T,Err}/p_T$	< 0.2
d_0	< 0.1 cm
I_{track}	< 10 GeV
I_{track}/E_T	< 0.2
I_{calo}	< 5 GeV

Table 5.1: Identified muon kinematic and isolation selection criteria [39].

For all three signals, we first require the presence of four non-isolated reconstructed leptons (four reconstructed electrons for $ZZ \rightarrow 4e$, four reconstructed muons for $ZZ \rightarrow 4\mu$, and two reconstructed electrons and muons for $ZZ \rightarrow 2e2\mu$). The next stage of cuts requires isolation for each lepton in terms of the isolation cuts associated with identified electrons and identified muons. For the $ZZ \rightarrow 4e$ analysis we loosen the I_{track}/p_T cut on the fourth electron, instead requiring $I_{track}/p_T < 1.0$, which helps boost signal with almost no increase in background. Then we cut on the sign of the lepton charges, requiring the total sum of the lepton charges to be zero. Our last cut requires the masses of the two reconstructed Z bosons to be between 70 GeV/c^2 and 110 GeV/c^2. The algorithm used matches the four leptons to the two Z bosons such that the sum of the squares of the differences in lepton pair mass and 90 GeV/c^2 is

minimized.

While all of our cuts improve the signal-to-background ratio, the requirement of isolation reduces background more than any other cut we impose. Our results are summarized in Tables 5.2, 5.3, and 5.4. Figure 5-4 also illustrates the reconstructed 4e mass of the $ZZ \rightarrow 4e$ signal and associated background after the first set of cuts (labeled as "electron reconstruction") and after all cuts are made (labeled as "electron identification"). For the signals, we calculate 4 counts/fb^{-1} for $ZZ \rightarrow 4e$, 5 counts/fb^{-1} for $ZZ \rightarrow 4\mu$, and 8 counts/fb^{-1} for $ZZ \rightarrow 2e2\mu$, yielding a total of 17 counts/fb^{-1} for $ZZ \rightarrow 4\ell$. In all three signal channels, we completely eliminate the background through our sequence of cuts. This may be indicative of our cuts being too tight. Further analysis may reveal that more signal can be retained with little background cost through the relaxation of some of these cuts. While we have no background to any of our signal samples, we can place an upper limit on background that is equivalent to one event of the highest cross section background channel, $Z \rightarrow 2e$. This implies an upper limit of 2.89 background counts/fb^{-1}, which is a very conservative result. Monte Carlo samples with more events are required for a better determination of this value.

5.3 Cross Section

The final task at hand in terms of our $ZZ \rightarrow 4\ell$ analysis is to calculate cross sections for each signal and for the $ZZ \rightarrow 4\ell$ channel as a whole. These calculations make use of the results of signal versus background optimization that we performed above. The general formula for cross section is

$$\sigma = \frac{N - B}{f \mathcal{L} A \varepsilon}, \tag{5.1}$$

ZZ->4e Signal and Background Cut Progression [counts/fb^{-1}]									
Selections	**ZZ->4e**	**WZ**	**WW**	**ttbar**	**Z->2μ**	**Z->2e**	**Wγ**	**Zγ->2μ**	**Zγ->2e**
Total	18	1621	114300	830000	1616333	1616333	56210	1474	1474
4 Reco. Electrons $E_T > 7$ GeV $\|\eta\| < 2.5$ etc.	6 (33.3 %) [33.3 %]	0.438 (~ 0 %)	1.48 (~ 0 %)	173 (~ 0 %)	0 (0 %)	205 (~ 0 %)	0 (0 %)	0 (0 %)	0.0925 (~ 0 %)
Isolation $I_{calo} < 15$ I_{trk}/E_T: < 0.2 (3e) < 1.0 (1e)	5 (83.3 %) [27.8 %]	0.236 (53.9 %)	0 (0 %)	0.394 (0.2 %)	0 (N/A)	8.68 (4.2 %)	0 (N/A)	0 (N/A)	0.0154 (16.7 %)
Charge 2 e^+, 2 e^-	4 (80.0 %) [22.2 %]	0.168 (71.2 %)	0 (N/A)	0.394 (100 %)	0 (N/A)	2.89 (33.3 %)	0 (N/A)	0 (N/A)	0.00771 (50.0 %)
Z Mass M_Z: > 70 GeV/c^2 < 110 GeV/c^2	4 (100 %) [22.2 %]	0 (0 %)	0 (N/A)	0 (0 %)	0 (N/A)	0 (0 %)	0 (N/A)	0 (N/A)	0 (0 %)

Table 5.2: Cut progression for $ZZ \rightarrow 4e$ signal and background. The relative number of counts remaining after each cut is shown in blue while the cumulative relative number of counts remaining is shown in red.

ZZ->4μ Signal and Background Cut Progression [counts/fb^{-1}]									
Selections	**ZZ->4μ**	**WZ**	**WW**	**ttbar**	**Z->2μ**	**Z->2e**	**Wγ**	**Zγ->2μ**	**Zγ->2e**
Total	18	1621	114300	830000	1616333	1616333	56210	1474	1474
4 Reco. Muons $E_T > 7$ GeV $\|\eta\| < 2.5$ etc.	11 (61.1 %) [61.1 %]	0.276 (~ 0 %)	0.980 (~ 0 %)	232 (~ 0 %)	104 (~ 0 %)	0 (0 %)	0 (0 %)	0.00780 (~ 0 %)	0 (0 %)
Isolation $I_{calo} < 5$ $I_{trk} < 10$ $I_{trk}/E_T < 0.2$	8 (72.7 %) [44.4 %]	0.0680 (24.6 %)	0 (0 %)	0 (0 %)	0 (0 %)	0 (N/A)	0 (N/A)	0.00390 (50.0 %)	0 (N/A)
Charge 2 μ^+, 2 μ^-	8 (100 %) [44.4 %]	0 (0 %)	0 (N/A)	0 (N/A)	0 (N/A)	0 (N/A)	0 (N/A)	0.00390 (100 %)	0 (N/A)
Z Mass M_Z: > 70 GeV/c^2 < 110 GeV/c^2	5 (62.5 %) [27.8 %]	0 (N/A)	0 (N/A)	0 (N/A)	0 (N/A)	0 (N/A)	0 (N/A)	0 (0 %)	0 (N/A)

Table 5.3: Cut progression for $ZZ \rightarrow 4\mu$ signal and background. The relative number of counts remaining after each cut is shown in blue while the cumulative relative number of counts remaining is shown in red.

ZZ->2e2μ Signal and Background Cut Progression [counts/fb^{-1}]									
Selections	**ZZ->2e2μ**	**WZ**	**WW**	**ttbar**	**Z->2μ**	**Z->2e**	**Wγ**	**Zγ->2μ**	**Zγ->2e**
Total	36	1621	114300	830000	1616333	1616333	56210	1474	1474
2 Reco. Electrons, Muons $E_T > 7$ GeV $\lvert\eta\rvert < 2.5$ etc.	14 (38.9 %) [38.9 %]	0.620 (~ 0 %)	0.490 (~ 0 %)	919 (0.1 %)	340 (~ 0 %)	40.6 (~ 0 %)	0 (0 %)	0.160 (~ 0 %)	0.00370 (~ 0 %)
Isolation I_{calo}: < 5 (μ) < 15 (e) $I_{trk} < 10$ (μ) $I_{trk}/E_T < 0.2$	9 (64.3 %) [23.7 %]	0 (0 %)	0 (0 %)	0.390 (~ 0 %)	3.70 (1.1 %)	0 (0 %)	0 (N/A)	0.0117 (7.3 %)	0 (0 %)
Charge 1 μ^+, 1 μ^-, 1 e^+, 1 e^-	9 (100 %) [23.7 %]	0 (N/A)	0 (N/A)	0.390 (100 %)	0 (0 %)	0 (N/A)	0 (N/A)	0.00390 (33.3 %)	0 (N/A)
Z Mass M_Z: > 70 GeV/c^2 < 110 GeV/c^2	8 (88.9 %) [22.2 %]	0 (N/A)	0 (N/A)	0 (0 %)	0 (N/A)	0 (N/A)	0 (N/A)	0 (0 %)	0 (N/A)

Table 5.4: Cut progression for $ZZ \rightarrow 2e2\mu$ signal and background. The relative number of counts remaining after each cut is shown in blue while the cumulative relative number of counts remaining is shown in red.

where $N = S + B$, S is the total number of signal counts, B is the total number of background counts, f is the branching ratio of the process of interest, $\mathcal{L}$ is the integrated luminosity, A is the acceptance, and ε is the total efficiency. For our analysis, we use as a benchmark an integrated luminosity of 1 fb^{-1} for the calculation of cross sections and 392.2 fb^{-1} for the calculation of acceptances and efficiencies.

Acceptance is defined as the fraction of events that have the potential to be reconstructed as $ZZ \rightarrow 4\ell$ events. Such events are required to have four generator-level leptons with $E_T > 7$ GeV and $|\eta| < 2.5$, with each lepton matching to a calo-tower (for electrons) or track (for muons). Since this must use generator-level information, it must be calculated separately from efficiency. For $ZZ \rightarrow 4e$, acceptance is split into two distinct quantities:

$$A = A_{\text{fid}} A_{\text{tower}}, \tag{5.2}$$

where A_{fid} includes the fiducial kinematic cuts of E_T and η cuts and A_{tower} includes

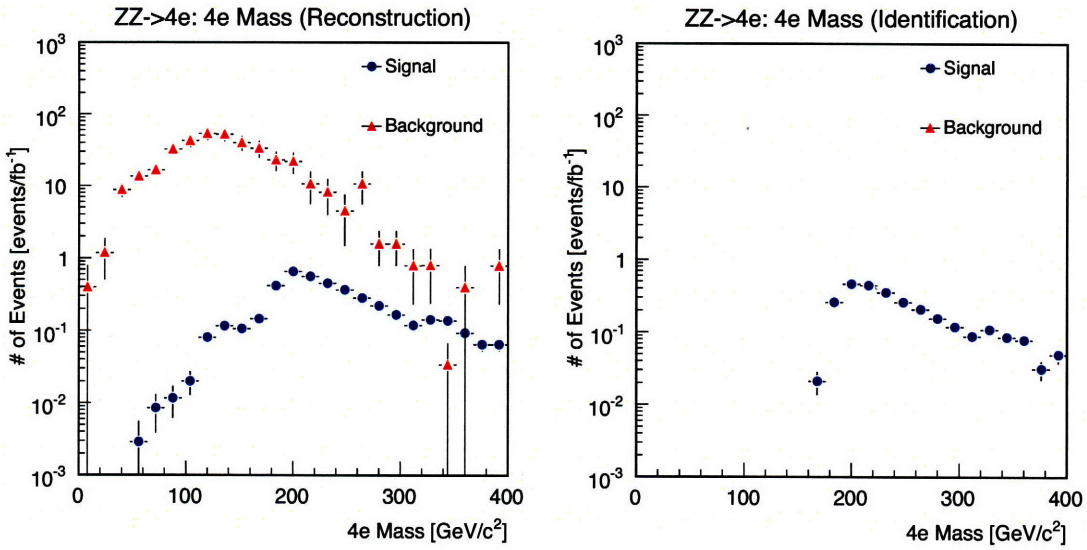

Figure 5-4: Reconstructed 4e mass of the $ZZ \rightarrow 4e$ signal and associated background after the first set of kinematic cuts (left) and after all cuts have been made (right). Note that the background is completely eliminated by applying all cuts.

the requirement of the leptons matching to calo-towers in the detector. Analogous quantities are defined for $ZZ \rightarrow 4\mu$ and $ZZ \rightarrow 2e2\mu$. The efficiencies are similarly split up into distinct quantities:

$$\varepsilon = \varepsilon_{\text{reco}} \varepsilon_{\text{iso}} \varepsilon_{\text{charge}} \varepsilon_{Z}, \tag{5.3}$$

where $\varepsilon_{\text{reco}}$ includes the requirement of four good reconstruction-level leptons, ε_{iso} includes isolation, $\varepsilon_{\text{charge}}$ includes restrictions on the lepton charges, and ε_{Z} includes the Z mass cut. It is important to note that in our analysis, we do not make use of the $Z \rightarrow 2e$ electron efficiencies and $Z \rightarrow 2\mu$ muon efficiencies, but instead use the data-like efficiencies calculated directly from the $ZZ \rightarrow 4\ell$ signal samples. These efficiencies are combined efficiencies of all four leptons, unlike the individual electron and muon efficiencies discussed above. When performing cross section calculations using actual data one should not make such a simplification and instead multiply together the individual lepton efficiencies, ε_e or ε_μ, calculated for electrons in the following section.

The acceptance and efficiency values that we find are presented in Tables 5.5, 5.6, and 5.7.

Because we are using a ZZ sample where the Z bosons are forced to decay into leptons, and because each lepton has nearly the same probability of being a decay product of each individual Z boson, the branching ratios are roughly 11.1%, 11.1%, and 22.2% for $ZZ \to 4e$, $ZZ \to 4\mu$, and $ZZ \to 2e2\mu$, respectively [40]. However, a slight correction has to be made due to the inclusion of tau particle intermediary states in our signal (e.g. $ZZ \to 2e2\tau \to 4e$). As a result, the branching ratios that we use in our cross section calculations are $f_{4e} = 11.8\%$, $f_{4\mu} = 11.8\%$, and $f_{2e2\mu} = 23.6\%$.

ZZ->4e Acceptance and Efficiency Measurements	
Acceptance	
$A_{fid} = 66.8\ \%$	$A = A_{fid}A_{tower} = 57.7\ \%$
$A_{tower} = 86.3\ \%$	
Efficiency	
$\varepsilon_{reco} = 44.5\ \%$	$\varepsilon = \varepsilon_{reco}\varepsilon_{iso}\varepsilon_{charge}\varepsilon_{Z} = 28.3\ \%$
$\varepsilon_{iso} = 85.7\ \%$	
$\varepsilon_{charge} = 93.8\ \%$	
$\varepsilon_{Z} = 79.1\ \%$	

Table 5.5: Acceptances and efficiencies for $ZZ \to 4e$.

Now we have determined all quantities that are inputs to the cross section calculation according to Equation 5.1. In order to calculate the uncertainties associated with these cross sections, we derive and make use of the following formulae:

$$\Delta\sigma_{\text{stat}} = \sigma\sqrt{\left(\frac{\Delta N}{N-B}\right)^2 + \left(\frac{\Delta B}{N-B}\right)^2 + \left(\frac{\Delta A}{A}\right)^2 + \left(\frac{\Delta\varepsilon}{\varepsilon}\right)^2} \tag{5.4}$$

and

$$\Delta\sigma_{\text{sys}} = \sigma\frac{\Delta\mathcal{L}}{\mathcal{L}}, \tag{5.5}$$

ZZ->4μ Acceptance and Efficiency Measurements	
Acceptance	
A_{fid} = 67.8 %	$A = A_{fid}A_{track}$ = 65.8 %
A_{track} = 97.1 %	
Efficiency	
ε_{reco} = 89.4 %	$\varepsilon = \varepsilon_{reco}\varepsilon_{iso}\varepsilon_{charge}\varepsilon_Z$ = 50.1 %
ε_{iso} = 73.4 %	
ε_{charge} = 99.9 %	
ε_Z = 76.5 %	

Table 5.6: Acceptances and efficiencies for $ZZ \rightarrow 4\mu$.

ZZ->2e2μ Acceptance and Efficiency Measurements	
Acceptance	
A_{fid} = 66.4 %	$A = A_{fid}A_{calo/track}$ = 60.5 %
$A_{calo/track}$ = 91.1 %	
Efficiency	
ε_{reco} = 63.2 %	$\varepsilon = \varepsilon_{reco}\varepsilon_{iso}\varepsilon_{charge}\varepsilon_Z$ = 32.8 %
ε_{iso} = 68.0 %	
ε_{charge} = 97.5 %	
ε_Z = 78.4 %	

Table 5.7: Acceptances and efficiencies for $ZZ \rightarrow 2e2\mu$.

where $\Delta\sigma_{\text{stat}}$ and $\Delta\sigma_{\text{sys}}$ are the statistical and systematic uncertainties on the cross section of interest, respectively. We assume that the systematic uncertainty of the luminosity is given by $\Delta\mathcal{L}/\mathcal{L} \approx 0.05$, though $\Delta\mathcal{L}$ will be better calculated after the LHC beam starts running [35]. The statistical uncertainty of the luminosity can be neglected as it is much smaller than the systematic uncertainty. Through the use of Equations 5.1, 5.4, and 5.5, we find $\sigma_{ZZ\rightarrow 4e} = 24.5 \pm 12.3 \pm 1.2$ fb, $\sigma_{ZZ\rightarrow 4\mu} = 15.2 \pm 6.8 \pm 0.8$ fb, and $\sigma_{ZZ\rightarrow 2e2\mu} = 40.3 \pm 14.3 \pm 2.0$ fb for the three signal cross sections. Note that statistical uncertainty is listed before systematic uncertainty for the cross sections. For the overall $ZZ \rightarrow 4\ell$ cross section, we find $\sigma_{ZZ\rightarrow 4\ell} = 180 \pm 45 \pm 6$ fb. All of these measured cross sections match up to their theoretical values (18.1

fb, 18.1 fb, 36.1 fb, and 153 fb, respectively [40]) within uncertainty bounds, but not with unreasonable precision. This suggests that we have correctly accounted for the uncertainty in our measurement. It is important to note that there will likely be additional systematic uncertainty associated with detector imperfections to account for when it comes time to use actual data.

5.4 Efficiency Application

With electron efficiencies computed from our electron identification studies above, we can now apply them to our $ZZ \rightarrow 4e$ analysis. If there is sufficient agreement between the $Z \rightarrow 2e$ and $ZZ \rightarrow 4e$ samples in terms of efficiency parameterized in E_{T}, then we can use the reconstruction-level $Z \rightarrow 2e$ electron efficiencies for $ZZ \rightarrow 4e$ analysis once the LHC begins running. This is very beneficial, since $Z \rightarrow 2e$ has a much higher cross section and as a result yields many more events than $ZZ \rightarrow 4e$. The larger number of events places lower statistical uncertainties on the efficiency calculation that in turn reduces the systematic uncertainty on the $ZZ \rightarrow 4e$ calculated cross section. The alternative would be to find a scale-factor by comparing $Z \rightarrow 2e$ efficiency in Monte Carlo to $Z \rightarrow 2e$ efficiency in data, and applying that same scale-factor to the $ZZ \rightarrow 4e$ efficiency in Monte Carlo to determine the efficiency in data for that signal.

In Figure 5-5 the reconstructed $ZZ \rightarrow 4e$ electron efficiency is compared to the $Z \rightarrow 2e$ electron efficiency. The comparison requires using a scaling function (also shown in Figure 5-5) to compare the efficiencies in terms of the same parameter, calo-tower-sum E_{T}. The nice agreement between the two distributions suggests that the $Z \rightarrow 2e$ electron efficiencies can be used in place of $ZZ \rightarrow 4e$ electron efficiencies in $ZZ \rightarrow 4e$ analysis using actual data. The same substitution may be possible for muon efficiencies in $ZZ \rightarrow 4\mu$ and $ZZ \rightarrow 2e2\mu$ analysis after an analogous comparison is made between efficiencies in these signals and muon efficiencies from $Z \rightarrow 2\mu$ samples.

Furthermore, in all cases, it is much better to use efficiencies parameterized in both E_{T} and η for higher accuracy. As an approximation in our cross section calculations, for each efficiency we only use one value that is averaged over all parameters.

Note that all efficiencies that we have computed here are for single electrons. In order to compute the total four electron efficiency that is a parameter in the cross section calculation, one must use $\varepsilon = \varepsilon_e^4$, where ε_e is the single electron efficiency discussed in this section. This assumes that there is no correlation between the efficiencies of the different electrons in the event, which is a reasonable assumption as the electrons are reconstructed independently and the efficiencies are calculated in separate p_{T} and η bins.

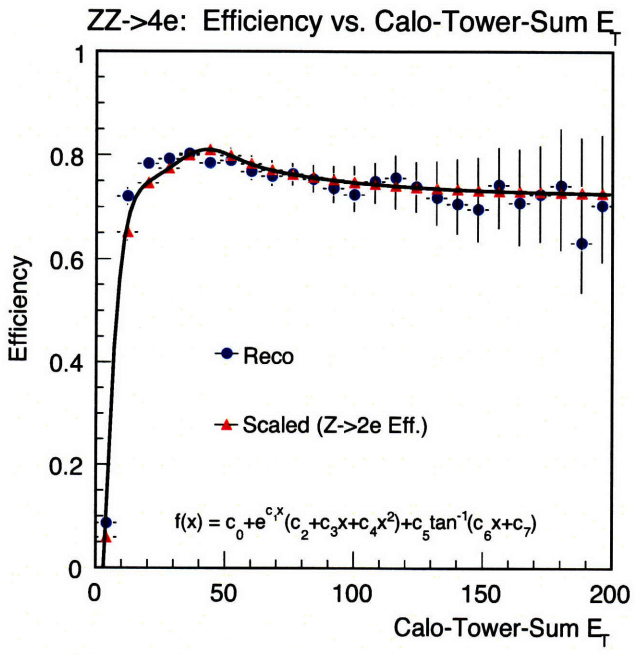

Figure 5-5: Comparison of $ZZ \rightarrow 4e$ and $Z \rightarrow 2e$ single electron efficiencies, parameterized in terms of calo-tower-sum E_{T}. There is very good agreement between the two distributions. Note the use of the scaling function to compare the two samples using the same parameter.

5.5 Fake Rate Application

Another correction that we must apply to our $ZZ \rightarrow 4e$ analysis is through the application of electron fake rates that we calculated above. Electron fake rates from the photon jet and QCD samples are applied to the background associated with the $ZZ \rightarrow 4e$ signal in order to remove background events in which there are electron fakes. However, in our case, we have no background left after the series of cuts that we apply. Furthermore, we have found the electron fake rate to be extremely small, on the order of 10^{-3}. Because of these two results, we can not directly apply the electron fake rates we calculated to our $ZZ \rightarrow 4e$ analysis. Cut relaxation would likely necessitate correction with fake rates due to increased background. Note that corrections could in theory also be made to the $ZZ \rightarrow 4\mu$ and $ZZ \rightarrow 2e2\mu$ samples once muon fake rates are calculated, though not in our case since we also find no background for these signals. Corrections using fake rates are much more important in other analyses, such as $WW \rightarrow 2l2\nu$ and $WZ \rightarrow 3l1\nu$, where there is much more background present.

Chapter 6

Conclusion

In our electron identification and $ZZ \rightarrow 4\ell(e,\mu)$ analyses, we have successfully developed techniques on the reconstruction level that can be applied once the LHC beam begins running later this year. In the $Z \rightarrow 2e$ channel we find an overall electron efficiency of $77.0\% \pm 1.3\%$ that can be applied to the $ZZ \rightarrow 4e$ signal channel, as well as an electron-pair charge misidentification rate of $3.0\% \pm 0.3\%$. Electron fake rates are calculated to be $(1.7 \pm 0.5) \cdot 10^{-3}$ for the photon jet channel and $(0.6 \pm 0.2) \cdot 10^{-3}$ for the QCD channel. For the $ZZ \rightarrow 4\ell$ signals, we calculate 4 counts/fb^{-1} for $ZZ \rightarrow 4e$, 5 counts/fb^{-1} for $ZZ \rightarrow 4\mu$, and 8 counts/fb^{-1} for $ZZ \rightarrow 2e2\mu$, yielding a total of 17 counts/fb^{-1} for $ZZ \rightarrow 4\ell$. For the three signal cross sections, we find $\sigma_{ZZ \rightarrow 4e} = 24.5 \pm 12.3 \pm 1.2$ fb, $\sigma_{ZZ \rightarrow 4\mu} = 15.2 \pm 6.8 \pm 0.8$ fb, and $\sigma_{ZZ \rightarrow 2e2\mu} = 40.3 \pm 14.3 \pm 2.0$ fb (with statistical uncertainty listed before systematic uncertainty). For the overall $ZZ \rightarrow 4\ell$ cross section, we find $\sigma_{ZZ \rightarrow 4\ell} = 180 \pm 45 \pm 6$ fb.

Bibliography

[1] S. Weinberg. *The First Three Minutes.* Basic Books, 1977.

[2] P. Higgs. *Broken Symmetries and the Masses of Gauge Bosons.* Phys. Rev. Lett., 13(16):508–509, 1964.

[3] F. Englert and R. Brout. *Broken Symmetry and the Mass of Gauge Vector Mesons.* Phys. Rev. Lett., 13(9):321–323, 1964.

[4] S. Glashow. *Partial Symmetries of Weak Interactions.* Nucl. Phys., 22:579–588, 1961.

[5] S. Weinberg. *A Model of Leptons.* Phys. Rev. Lett., 19:1264–1266, 1967.

[6] A. Salam. *Elementary Particle Physics: Relativistic Groups and Analyticity.* In N. Svartholm, editor, Nobel Symposium No. 8, page 367, Stockholm, 1968. Almquist and Wiksell.

[7] J. Wess and B. Zumino. *A Lagrangian Model Invariant Under Supergauge Transformations.* Phys. Lett. B, 49:52–54, 1974.

[8] E. Witten. *Mass Hierarchies in Supersymmetric Theories.* Phys. Lett. B, 105:267–271, 1981.

[9] I. Antoniadis. *A Possible New Dimension at a Few TeV.* Phys. Lett. B, 246:377–384, 1990.

[10] M. Green, J. Schwarz, and E. Witten. *Superstring Theory.* Cambridge University Press, Cambridge, 1987.

[11] J. Pati and A. Salam. *Lepton Number as the Fourth "Color".* Phys. Rev. D, 10(1):275–289, 1974.

[12] H. Georgi and S. Glashow. *Unity of All Elementary-Particle Forces.* Phys. Rev. Lett., 32(8):438–441, 1974.

[13] N. Arkani-Hamed, S. Dimopoulos, and G. Dvali. *The Hierarchy Problem and New Dimensions at a Millimeter.* Phys. Lett. B, 429:263–272, 1998.

[14] C. Harris. *Exploring Higher Dimensional Black Holes at the Large Hadron Collider.* J. High Energy Phys., 505:53, 2005.

[15] M. Veltman. *Facts and Mysteries in Elementary Particle Physics.* World Scientific Publishing, 2003.

[16] T. Sjöstrand, S. Mrenna, and P. Skands. *PYTHIA 6.4 Physics and Manual.* J. High Energy Phys., 5(26), 2006.

[17] *Geant4 Physics Manual,* http://cern.ch/geant4/support/userdocuments.shtml, June 2007.

[18] CMS Collaboration. *CMS Technical Design Report, Volume II: Physics Performance.* J. Phys. G: Nucl. Part. Phys., 34(6):995–1579, June 2007.

[19] P. Dirac. *The Quantum Theory of the Electron.* Proc. R. Soc. Lond. A, 117:610–612, 1928.

[20] D. Green. *High P_T Physics at Hadron Colliders.* Cambridge University Press, 2005.

[21] W. Atwood. *Lectures on Lepton Nucleon Scattering and Quantum Chromodynamics.* In *Progress in Physics*, volume 4, 1982.

[22] J. Friedman. *Deep Inelastic Scattering: Comparisons with the Quark Model.* Nobel Lecture, December 1990.

[23] H. Kendall. *Deep Inelastic Scattering: Experiments on the Proton and the Observation of Scaling.* Nobel Lecture, December 1990.

[24] R. Taylor. *Deep Inelastic Scattering: The Early Years.* Nobel Lecture, December 1990.

[25] F. Halzen and A. Martin. *Quarks and Leptons.* Wiley, 1984.

[26] D. Griffiths. *Introduction to Elementary Particles.* Wiley, 1987.

[27] D. Gross and F. Wilczek. *Ultraviolet Behavior of Non-Abelian Gauge Theories.* Phys. Rev. Lett., 30(26):1343–1346, 1973.

[28] H. Politzer. *Reliable Perturbative Results for Strong Interactions?* Phys. Rev. Lett., 30(26):1346–1349, 1973.

[29] B. Povh, K. Rith, C. Scholz, and F. Zetsche. *Particles and Nuclei.* Springer, 2006.

[30] UA1 Collaboration. *Experimental Observation of Isolated Large Transverse Energy Electrons with Associated Missing Energy at* $\sqrt{s} = 540$ *GeV.* Phys. Lett. B, 122(1):103–116, 1983.

[31] UA2 Collaboration. *Observation of Single Isolated Electrons of High Transverse Momentum in Events with Missing Transverse Energy at the CERN* $\bar{p}p$ *Collider.* Phys. Lett. B, 122:476–485, 1983.

[32] G. 't Hooft. *Renormalizable Lagrangians for Massive Yang-Mills Fields.* Nucl. Phys. B, 35:167–188, 1971.

[33] G. 't Hooft and M. Veltman. *Regularization and Renormalization of Gauge Fields.* Nucl. Phys. B, 44:189–213, 1972.

[34] ALEPH Collaboration, DELPHI Collaboration, L3 Collaboration, OPAL Collaboration, and The LEP Working Group for Higgs Boson Searches. *Search for the Standard Model Higgs Boson at LEP.* Phys. Lett. B, 565:61–75, 2003.

[35] CMS Collaboration. *CMS Technical Design Report, Volume I: Detector Performance and Software.* Technical Report CERN/LHCC 2006-001, CERN, 2006.

[36] CMS Collaboration. *CMS Tracker Technical Design Report.* Technical Report CERN/LHCC 98-6, CERN, 1998.

[37] CMS Collaboration. *CMS Electromagnetic Calorimeter Technical Design Report.* Technical Report CERN/LHCC 97-33, CERN, 1997.

[38] CMS Collaboration. *CMS Muon Technical Design Report.* Technical Report CERN/LHCC 97-32, CERN, 1997.

[39] C. Melachrinos. *The Muon Detection System and $WZ \rightarrow 3\ell(e,\mu)$ Cross Section Measurement at CMS.* MIT Bachelor of Science Thesis, 2008.

[40] W.-M. Yao, et al. *Review of Particle Physics.* J. Phys. G: Nucl. Part. Phys., 33:1–1232, 2006.